



UNIVERSITY*of*
TASMANIA

**Development and Simulation of a Traction Control System Using
Individual Motor Direct Torque Control Techniques for a Formula
SAE Electric Racing Vehicle**

Pengcheng Ji

School of Engineering

B.Eng. (Hons), University of Tasmania

Supervised by:

Dr Jason Lavroff

Dr Peter Doe

Prof. Michael Negnevitsky

A thesis submitted in fulfillment of the requirements for the degree of Master of
Engineering Science

University of Tasmania

November 2020

Declaration and Statements

Declaration of Originality

This thesis contains no material which has been accepted for a degree or diploma by the University or any other institution, except by way of background information and duly acknowledged in the thesis, and to the best of my knowledge and belief no material previously published or written by another person except where due acknowledgement is made in the text of the thesis, nor does the thesis contain any material that infringes copyright.

Authority of Access

This thesis may be made available for loan and limited copying and communication in accordance with the Copyright Act 1968.

Statement regarding Published Work contained in Thesis

The publishers of the papers comprising Chapters 4 hold the copyright for that content and access to the material should be sought from the respective journals. The remaining non published content of the thesis may be made available for loan and limited copying and communication in accordance with the Copyright Act 1968.

Signed: _____

Name: Pengcheng Ji

Date: 24/11/2020

Statement of Co-Authorship

The following people and institutions contributed to the publication of the work undertaken as part of this thesis:

- **Candidate - Pengcheng Ji,** *Master by Research Candidate*

School of Engineering, University of Tasmania

- **Author 1 - Dr. Jason Lavroff,** *Primary Supervisor*

School of Engineering, University of Tasmania

- **Author 2 - Dr. Peter Doe,** *Co-supervisor*

School of Engineering, University of Tasmania

- **Author 3 - Prof. Michael Negnevitsky,** *Co-supervisor*

School of Engineering, University of Tasmania

- **Author 4 - Dr. Timothy Gale,** *Co-supervisor*

School of Engineering, University of Tasmania

- **Author 5 - Sheran Nanayakkara.,** *Honour student*

School of Engineering, University of Tasmania

Contribution of work by co-authors for each paper:

Paper 1: Located in Chapter 4.

Pengcheng Ji, Sheran Nanayakkara, Jason Lavroff, Michael Negnevitsky, Peter Doe, Timothy Gale “Design and Simulation Analysis of a Formula SAE Electric Vehicle Propulsion System,” *Veh. Technol. Eng.*, no. 873UA055, pp. 16-20,22-24, 2017.

Author contributions:

This paper has been published and received 2016 Mobility Engineering Excellence Awards(Finalist Student Award).

The candidate contributed to the planning and execution of the research project, experimental practice, data analysis and drafted the paper. Author 1, Author 2, Author 3 and Author 4 contributed to the conception and design of the project, also paper refinement, review and final approval. Author 5 contributed to data acquisition, analysis and paper drafting.

We, the undersigned, endorse the above stated contribution of work undertaken for each of the published (or submitted) peer-reviewed manuscripts contributing to this thesis:

Signed: _____ **Date:** 13/11/2020

Candidate: Pengcheng Ji
School of Engineering
University of Tasmania

Signed: _____ **Date:** 16/11/2020

Primary Supervisor: Dr. Jason Lavroff
School of Engineering
University of Tasmania

Signed: _____ **Date:** 18th November 2020

Head of School: Prof. Andrew Chan
School of Engineering
University of Tasmania

Acknowledgements

I wish to express my sincerest appreciation to my supervisory team, my primary supervisor Dr Jason Lavroff, my co-supervisors Prof. Michael Negnevitsky and Dr Peter Doe. I felt incredibly grateful for their continuous and invaluable support throughout my candidature.

I can not thank you enough, Dr Jason Lavroff, we knew each other from 8 years ago when we were overseas, and you have been supporting me both academically and personally since I arrived in Australia to begin my study. My master project would not become a reality without your guidance, support and contribution. I have been through many ups and downs in my professional and personal life during this master candidature, but you were always there to guide me and offer advice.

I am also privileged and honoured to work with Prof Michael Negnevitsky. I would like to thank him for sharing his rich experience, knowledge and wisdom which help me to improve on my time management, project planning and academic writing skills. The practical and strategic approach he has taught me to overcome different obstacles was a life lesson for me.

I am very extremely grateful for the advice and support Dr Peter Doe offered at the different stages of my candidature and he also helped me so much on formatting the thesis and optimise the presentation of my works.

Additionally, I would like to thank Dr Timothy Gale and Dr David Warren for their support and suggestions at the early stage of the project.

Thanks to all of my teammates from UTAS FSAE team who have pushed me out of my comfort zone and I appreciate the opportunity to collaborate with such talented people from different disciplines to deliver a challenging project.

Finally, I sincerely wish to thank my wife Le Wang and my other family members.

Pursuing this master degree has not been an easy task, we have faced lots of challenges together. Balancing between a full-time job, study and life, financial pressure, surgery and many more. I am grateful that I have you around me and I look forward to spending more quality time with my family.

Pengcheng Ji

Abstract

Independent-drive electric vehicles represent an advanced approach to vehicle dynamic control. The main feature of these systems is that they use traction motors that are independently connected to each wheel. This results in a shorter driveline, higher transmission efficiency, more compact packaging, and better utilisation of space. Combined with the torque information produced by electric traction motors, an independent-drive electric vehicle system is capable of performing traction control, anti-lock braking control and electronic power steering. Traction control is also an effective strategy to control longitudinal vehicle dynamics that functions by preventing the wheels from slipping while driving. It has potential for optimising vehicle dynamics during frequent acceleration and takeoff. Since the late 1990s, there have been several studies regarding traction control for fully electric motor drive vehicles. These studies have investigated traction control systems based on fuzzy methods, rule-based control, sliding-mode control, Proportional–Integral–Derivative control and modification, optimal linearisation control and model-based control. A further distinction can be made between torque-based control, slip-based control and systems that combine both. Nevertheless, most of the existing studies of torque-based traction control have been investigated only in simulation. Further, since 2012, only four studies have focused on designing an electric motor controller with an embedded traction control algorithm. The aim of this project is to understand and develop a traction control system that can be used for the future University of Tasmania Formula SAE electric racing vehicle. Following the guidelines of the Formula SAE rules, the vehicle will be an 80 kW, 600 V peak, rear-wheel drive, open-wheel formula race vehicle.

Contents

Declaration and Statements	i
Statement of Co-Authorship	ii
Acknowledgements.....	iv
Abstract.....	vi
Contents	vii
List of Figures.....	ix
List of Tables	xi
Chapter 1: Introduction	1
1.1 Background	1
1.2 Formula SAE and University of Tasmania Motorsport Engineering	3
1.3 Research Objectives and Contribution	4
1.4 Thesis Outline.....	4
Chapter 2: State-of-the-Art Electric Vehicle Traction Control.....	6
2.1 Electric Vehicle Traction Control System Architecture.....	6
2.1.1 Friction model.....	6
<i>2.1.1.1 Static friction model</i>	<i>6</i>
<i>2.1.1.2 Coulomb friction model</i>	<i>6</i>
<i>2.1.1.3 Dynamic friction model.....</i>	<i>7</i>
2.1.2 Tyre model.....	8
2.1.3 Vehicle model.....	9
<i>2.1.3.1 Quarter-vehicle models.....</i>	<i>10</i>
2.2 Electric Motor Control System.....	11
2.2.1 Background.....	11
2.2.2 Common structures of permanent-magnet synchronous motors	13
<i>2.2.2.1 Radially placed buried-magnet structures</i>	<i>14</i>
<i>2.2.2.2 Circular buried-magnet structures</i>	<i>15</i>
2.2.3 Vector control schemes for permanent-magnet synchronous motors.....	15
<i>2.2.3.1 $id = 0$ control.....</i>	<i>18</i>
<i>2.2.3.2 Maximum torque-per-ampere control.....</i>	<i>18</i>
<i>2.2.3.3 Unity power factor control.....</i>	<i>19</i>
<i>2.2.3.4 Field-weakening control</i>	<i>19</i>
2.2.4 Direct torque control of permanent-magnet synchronous motors for electric vehicles	20
Chapter 3: Mathematical Model for the Electric Vehicle Traction Control System	22
3.1 Mathematical Modelling of Permanent-Magnet Synchronous Motors	22
3.2 Direct Torque Control of Permanent-Magnet Synchronous Motors	24
3.2.1 Flux linkage and torque with a voltage source inverter.....	26
3.2.2 Direct torque control interior permanent-magnet drive control scheme with look-up table technique	29
3.2.3 Stability criteria	30
3.2.4 Direct torque control scheme for maximum torque-per-ampere trajectory control.....	32
3.3 Indirect Torque Control of an Interior Permanent-Magnet Synchronous Motor Drive.....	32

3.3.1 Stator current trajectories under current control	33
3.3.2 Maximum torque-per-ampere trajectory.....	34
3.3.3 Voltage and current constraints trajectory	34
3.3.4 Voltage-limited maximum output trajectory	36
3.3.5 Control mode selection.....	36
3.3.5.1 <i>Speed below the base speed</i>	37
3.3.5.2 <i>Speed above crossover speed</i>	38
3.3.5.3 <i>Speed between base speed and crossover speed</i>	38
Chapter 4: Design and Simulation of a Formula SAE Electric Vehicle	
Propulsion System.....	39
4.1 Introduction	39
4.2 Propulsion System Architecture	40
4.3 Basic Vehicle Parameters	41
4.4 Propulsion System Design Methodology	43
4.4.1 Electric motor drive system	43
4.4.2 Transmission.....	46
4.4.3 Gearbox design	49
4.5 Simulation Analysis of the Powertrain.....	51
Chapter 5: Simulation Study of the Traction Control System	56
5.1 Simulation Studies of the Direct Torque Control Interior Permanent-Magnet Drive.....	56
5.2 Basic Problems Associated with Direct Torque Control for Permanent-Magnet Synchronous Motors and Improvements	61
5.2.1 Stator resistance variation.....	61
5.2.2 Non-linear effects by inverter characteristic.....	61
5.2.3 Offset errors in measurement of voltage and current	61
5.2.4 Initial rotor position estimation	62
5.2.5 Unacceptable ripples in torque and flux linkage	62
5.3 Simulation Studies of Indirect Torque Controlled Interior Permanent-Magnet Drives	63
5.4 Development of the Motor Control Test Bench.....	74
Chapter 6: Conclusion and Future Research	76
6.1 Conclusions	76
6.2 Future Research.....	77
6.2.1 Simulation works	77
6.2.2 Physical data collection and comparison study	77
References	79

List of Figures

Figure 2.1. Static friction phenomena[18]	6
Figure 2.2. a) point contact, lumped model. b) contact patch, distributed model [21].	7
Figure 2.3. Typical tyre/road friction profiles for varied road condition and vehicle velocity [24].	9
Figure 2.4. Quarter-vehicle suspension model [26].	10
Figure 2.5. Quarter-vehicle longitudinal model [27].	11
Figure 2.6. Typical rotor cross-sections of permanent-magnet synchronous motors [39].	14
Figure 2.7. Radially placed buried-magnet structure [40].	15
Figure 2.8. Circular buried-magnet structure [40].	15
Figure 3.1. The stator and rotor flux linkages directions on different reference frames	24
Figure 3.2. Two-level voltage source inverter and a three-phase machine [29].	26
Figure 3.3. Eight voltage space vectors combined by the two-level VSU [39].	27
Figure 3.4. Control of the stator flux linkage by applying voltage vectors [39].	30
Figure 3.5. Two roots of $f_x = 0$ with different λ_s [39].	31
Figure 3.6. Phase diagram of an interior permanent-magnet synchronous motor in a steady state [39].....	33
Figure 3.7. Current and voltage constraints trajectory and maximum torque-per-ampere trajectory of interior permanent-magnet motor [39].	35
Figure 3.8. Maximum torque-per-ampere, current and voltage limit trajectories on the d-q plane[39].....	37
Figure 3.9. Maximum torque-per-ampere, current and voltage limit trajectories on the d-q plane [29].....	37
Figure 4.1. Electric vehicle powertrain structure.	41
Figure 4.2. Motor drive system.	46
Figure 4.3. Overview of propulsion system.	50
Figure 4.4. Proposed gearbox design.	50
Figure 4.5. Finite element analysis of the gearbox.	51
Figure 4.6. Contour plot of on-track power consumption.....	52
Figure 4.7. On-track power consumption as a function of elapsed distance.....	52
Figure 4.8. On-track speed variation.....	53
Figure 4.9. Variations in on-track rpm with elapsed distance.....	53
Figure 5.1. Block diagram of the look-up table for the direct torque controlled interior permanent-magnet drive.	56
Figure 5.2. Flow chart for the conventional permanent-magnet synchronous motor, direct torque control system.	57

Figure 5.3. Stator current, motor speed and torque response.....	59
Figure 5.4. Flux linkage for d and q components.	60
Figure 5.5. Locus of the stator flux linkage under direct torque control scheme.	60
Figure 5.6. Block diagram of the interior permanent-magnet synchronous motor drive.....	63
Figure 5.7. Torque limitation block.	65
Figure 5.8. Detailed model of the interior permanent-magnet synchronous motor drive.....	65
Figure 5.9. Mathematical model for the electric motor.	66
Figure 5.10. Detailed model of the vector controller.	66
Figure 5.11. Detailed model of the speed controller.....	67
Figure 5.12. Simulation results at constant speed.	69
Figure 5.13. Power output at constant speed.....	70
Figure 5.14. i_q current vector response.....	70
Figure 5.15. i_d current vector response.....	71
Figure 5.16. Locus of both current vectors.	71
Figure 5.17. Simulation results at constant torque reference.	72
Figure 5.18. Mechanical power at constant load torque.	73
Figure 5.19. i_d current response.....	73
Figure 5.20. i_q current response.....	73
Figure 5.21. Locus of i_d and i_q vectors.	74
Figure 5.22. University of Tasmania Formula SAE motor bench test platform.	74

List of Tables

Table 3.1 <i>Flux linkage and torque control under direct torque control [39]</i>	29
Table 4.1 <i>Basic vehicle parameters of 2015 UTAS FSAE vehicle</i>	42
Table 4.2 <i>Key performance indicators of the vehicle</i>	43
Table 4.3 <i>Electric motor parameters</i>	44
Table 4.4 <i>Weighted decision matrix for selection of reduction mechanism</i>	47
Table 4.5 <i>Safety factors of all analysed gearbox components</i>	51
Table 5.1 <i>The $\alpha\beta$ components of the non-zero voltage vectors [39]</i>	58
Table 5.2 <i>Parameters in direct torque control interior permanent-magnet drive modelling</i>	58
Table 5.3 <i>Step functions for load torque</i>	59
Table 5.4 <i>Input speed reference</i>	64
Table 5.5 <i>Input torque reference</i>	64
Table 5.6 <i>Parameters of the interior permanent-magnet drive and controllers</i>	68

Chapter 1: Introduction

1.1 Background

Independent-drive electric vehicles (EV) represent an advanced approach to dynamic vehicle control. The main feature of independent-drive systems is that they use traction motors that are independently connected to each wheel. This results in a shorter driveline, higher transmission efficiency, more compact packing and better utilisation of space. Combined with the torque information produced by electric traction motors, independent-drive EVs can perform effective traction control, anti-lock braking system control, and electronic power [1].

Traction control (TC) is an effective strategy for controlling longitudinal vehicle dynamics. TC prevents the wheels from skidding while driving, potentially optimising vehicle dynamics during periods of frequent acceleration and takeoff [2]. In conventional internal combustion vehicles, TC is achieved by employing friction brakes as actuators and/or by limiting driveline engine power. This method is effective if the friction properties of the road surface are different on the wheels on the same axis, but it faces the drawback of a decrease in power, which reduces outright acceleration. Conversely, even two-wheel-drive EVs can independently control the output of the electric motors to the wheels, providing maximum torque and traction to each tyre and improving handling and stability in a variety of situations [3]. Moreover, the acceleration performance of EVs can be up to 3 per cent greater than that of internal combustion vehicles[4].

Since the late 1990s, several works have been published regarding TC for fully electric motor drive vehicles. This literature has explored a variety of TC systems, including those using fuzzy methods, rule-based control, sliding-mode control, PID control and modification, optimal linearisation control and model-based control[2], [5]. Further differentiation can be made between approaches that use torque-based control and

slip-based control and those that use a combination of both. In most prior studies, torque-based TC was investigated only in simulation[2]. In addition , there have been three studies focused on designing an electric motor controller with an embedded TC algorithm since 2012[6]–[8]. There has only been one study on TC that was based on a Formula SAE (FSAE) vehicle[9].

One starting point for the development of TC is to consider the slip control of an individual wheel [10]. Slip control prevents wheels from locking during braking and spinning during acceleration. It involves systems that sense the state of the wheels and feed this information back to modulate the torque applied to each. As such, this study will be focused on an investigation of longitudinal vehicle dynamics.

Slip control methods vary depending on the sensor signals used and the assumptions made about the conditions under which the vehicle will operate. Conventionally, slip control has required the slip ratio(λ) to be estimated using the vehicle speed detected by sensors,:

$$\lambda = \frac{V_w - V}{V_w} \quad (1.1)$$

In this equation, V_w is wheel velocity and V is vehicle velocity. The desired slip ratio is obtained using the Magic Formula [11], a well-known empirical relationship between friction and slip. The slip controller uses the error between the estimated and desired slip ratio as feedback compensation. This process exists, in part, because slip control has evolved with internal combustion vehicle that cannot measure engine torque precisely. It is possible to obtain V from encoders on the none-driven wheels, accelerometers, optical sensors, magnetic marker sensors[10], and GPS[12] on the chassis. A more accurate vehicle speed can be estimated by using advanced filters to fuse multiple sensor signals[13]. In EVs, the ability to measure the torque from the electric motor makes it possible to estimate the slip ratio without measuring the vehicle speed[14]. Sliding-mode controllers can be used to deal with uncertain road conditions[15].

Alternatively, model-based approaches exist that only consider the dynamics of the wheel and therefore, do not depend on a static slip-friction relationship[16].

1.2 Formula SAE and University of Tasmania Motorsport Engineering

SAE International, formerly known as the Society of Automotive Engineers, launched the FSAE series of student vehicle design competitions in 1979. Students from universities around the world now participate in one or more FSAE competitions each year. In 2014, a total of nine FSAE competitions were held around the world.

The FSAE involves more than simply designing and building a race car; vehicles must be built according to specific standards, rules and regulations laid out by SAE International. Business considerations are incorporated into the competition, particularly in static events. The concept behind Formula SAE is that a fictional manufacturing company has contracted a design team to develop a small Formula-style race car. The prototype race car is to be evaluated for its potential as a production item. The target marketing group for the race car is the non-professional weekend autocross racer. Each student team designs, builds and tests a prototype based on a series of rules whose purpose is both to ensure onsite event operations and promote clever problem solving.[17]

In 2014, the University of Tasmania Motorsport Engineering (UME) team represented the University of Tasmania (UTAS) at the FSAE Australasia competition at Calder Park in Victoria. The UME intends to continue its involvement in FSAE by entering the Australasia competition on an annual basis with a short-term plan to convert an existing internal combustion car to an EV. This will not only provide further development for undergraduate students but will also lead to the establishment of a postgraduate research group primarily focused on developing EV technology that will be transferrable to several other industries.

1.3 Research Objectives and Contribution

The aim of this project was to understand and initiate the process of developing a TC system for an EV to be used in the future UTAS FSAE EV. In line with the FSAE rules, the vehicle will be an 80 kW, 600 V peak, rear-wheel drive, open-wheel formula race vehicle. A secondary aim was to develop a physical test platform to evaluate the real performance of TC methods using the 2017 UTAS FSAE EV powertrain.

There were four key objectives:

1. Perform a state-of-the-art literature review of EV TC systems.
2. Develop a control structure and mathematical model for a TC system.
3. Establish a simulation module in the MATLAB/SIMULINK environment to evaluate the performance of motor control and the TC algorithm.
4. Design and construct a physical test platform capable of testing the TC system.

1.4 Thesis Outline

This thesis is structured as follows:

- Chapter 1: This chapter provides background regarding EVs and TC and introduces the project background (the FSAE competition) and motivations.
- Chapter 2: This chapter presents the findings of a literature review regarding three major components relevant to developing an EV TC system:
 1. The vehicle system, including a friction model, tyre model and vehicle model.
 2. The motor control system consisting of a control algorithm, inverter and motor model.
 3. The TC system, including the controller and sensors.
- Chapter 3: This chapter provides a mathematical representation of the EV drivetrain system. It also explains different electric motor control technics and analyses the characteristics of the control method.

- Chapter 4: This chapter discusses the design and development of the FSAE electric vehicle. It provides a design method for an EV traction system and the simulation results used to evaluate the design.
- Chapter 5: This chapter presents the simulation and analysis results for the EV motor TC system. These results were based on the implementation of the motor control algorithm discussed in Chapters 2 and 3 in MATLAB/SIMULINK.
- Chapter 6: This chapter summarises the project and the progress made so far. It also identifies opportunities for future research to further understand the entire EV TC system.

Chapter 2: State-of-the-Art Electric Vehicle Traction Control

2.1 Electric Vehicle Traction Control System Architecture

2.1.1 Friction model

Friction can be used to create a variety of phenomena. There are two main models for monitoring friction: static friction models and dynamic friction models. Each modelling method can be used to monitor different characteristics of friction.

2.1.1.1 Static friction model

The static friction model is the most fundamental method for simulating the force characteristics of friction. This model only considers a body's steady-state velocity and the force applied. There are several versions of this model, as shown in Figure 2.1[18] and discussed below.

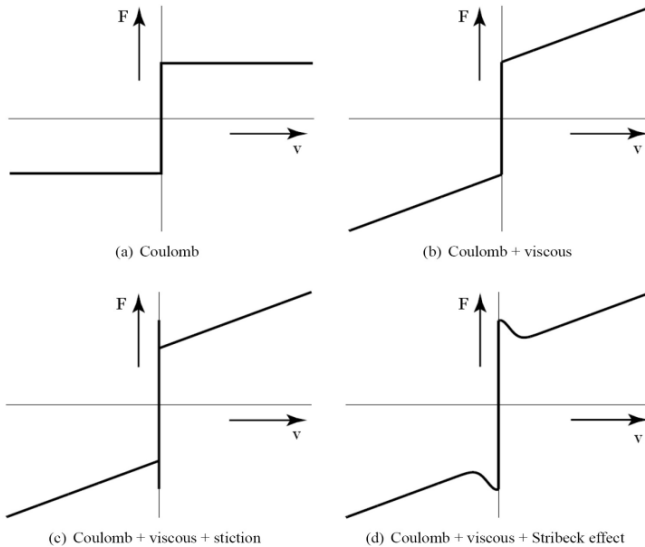


Figure 2.1. Static friction phenomena[18]

2.1.1.2 Coulomb friction model

In 1785, Coulomb discovered that the force of the friction between two bodies in contact is proportional to the normal force (N) not dependent on the contact patch. In dry

conditions, the characteristics of the two bodies in contact with relative motion can be described as follows:

$$F = -F_c \cdot \sin(\nu) \quad (2.1)$$

In this equation, F_c represents the Coulomb friction force and ν is the relative velocity between the bodies.

2.1.1.2.1 Stribeck effect

In the early 1920s, it was discovered that when static friction exceeds Coulomb friction, friction force can decrease as relative velocity increases. This is an effect of partial fluid lubrication [19]. The equation for friction force is as follows:

$$F = (F_s - F_c) \exp(|\nu/\nu_S|^{\delta_s}) \quad (2.2)$$

Here, ν_S is the Stribeck velocity and δ_s is the coefficient of the body form. The Stribeck effect can lead to stick-slip motion when a body is under friction [20].

2.1.1.3 Dynamic friction model

A dynamic friction model, which introduces a time variable, can further describe the characteristics of friction force.

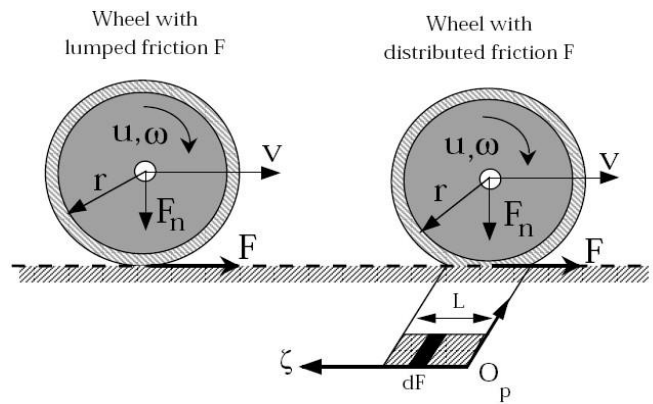


Figure 2.2. a) point contact, lumped model. b) contact patch, distributed model [21].

The static friction model can represent static phenomena (e.g., Coulomb, viscous, stiction and the Stribeck effect). These behaviours are captured by the classical model of friction; however, the usefulness of the model for control purposes is questionable in light of the discontinuity of zero velocity. Armstrong and Karnopp proposed models to

overcome this problem[22]. More recently, researchers have investigated the dynamic behaviour of friction. This research showed that dynamic friction has two components: hysteresis and a variable breakaway force behaviour. Several dynamic friction models have been developed to capture these additional phenomena. The majority of these—including the widely used LuGre model—are extensions of the Dahl model[23]. Combined with the simplicity of the Dahl model, this makes the Dahl model a good starting point for modelling friction [18].

2.1.2 Tyre model

Tyres are the only points of connection between vehicles and the ground and tyre performance has significant effects on vehicle dynamics. Complex tyre modelling is outside the scope of this study. Because this research concerns longitudinal motion on a flat road, the focus has been on the generation of friction force—an area that is largely covered by friction models. Further, most of the friction models considered are concerned with single points of contact; therefore, the deformation of the tyre has not been relevant. Discussion of tyre modelling is included in this chapter for completeness and to introduce the reader to the Magic Formula (MF) tyre model, which is, in its simplest form, a static friction model [11].

There are four types of tyre modelling [11]. The first consists of empirical models that are curve-fits to experimental data. These provide a high level of accuracy but offer limited explanations regarding the performance of the tyre. The best-known of these is the MF [11], which has become the standard of comparison for friction models. The MF fits a curve to steady-state experimental data like the curves shown in Figure 2.3 [24]. These data are generated under strictly controlled test conditions in which the velocity of the vehicle and the angular velocity of the wheel are independent of each other but closely coupled [25]. Despite this, static maps (such as those in Figure 2.3) provide no

understanding of the transition between different conditions—a constant consideration in the real world.

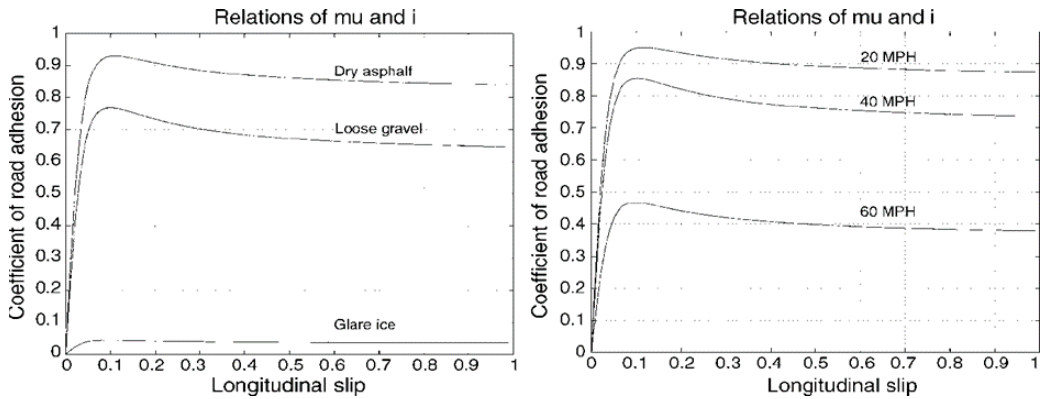


Figure 2.3. Typical tyre/road friction profiles for varied road condition and vehicle velocity [24].

The second type of tyre modelling comprises semi-empirical models that are still based on empirical data but contain structures related to physical models. The third type is made up of simplified physical models. These models provide an effective representation of major observed characteristics while simplifying the mathematics for the sake of efficient simulation. The fourth category consists of complex physical models, including finite-element models that can model individual tread elements. These are used for detailed analysis of tyres and can be computationally intensive. The first and fourth categories provide the greatest accuracy; conversely, the second and third categories are less complex and widely used in simulation.

2.1.3 Vehicle model

A vehicle model is a set of differential equations that represent a simplified mathematical model of a vehicle. Vehicle models are used to simulate real vehicles, reducing costs and time-consuming testing. It is critical that an appropriate model is used based on its applications and accuracy, as there are various types of vehicle models, each with their own assumptions. The complexity of a vehicle model is determined by the number of bodies it includes and the degrees of freedom they have.

The vehicle models put forth in the literature can be split into three broad categories: quarter-vehicle (QV), half-vehicle and full-vehicle models. This chapter will focus on QV for simplicity.

2.1.3.1 Quarter-vehicle models

QV models simulate a single wheel and a single vehicle mass. They only describe either vertical or longitudinal motion. The vertical QV model consists of a wheel mass and vehicle mass, each with a single degree of freedom. The masses are connected by a suspension model as shown in Figure 2.4. The suspension model contains a spring-damper and, optionally, an active component. The tyre is connected to the road by either a spring or a damper, representing the tyre's dynamics. This model is useful for simulating the motion of an individual suspension unit and analysing its performance relative to a varying road profile [26]. It does not include a suspension stop or a mechanism for wheel lift-off; as a result, it may not be able to simulate the vehicle's response to sudden road displacements like speed bumps.

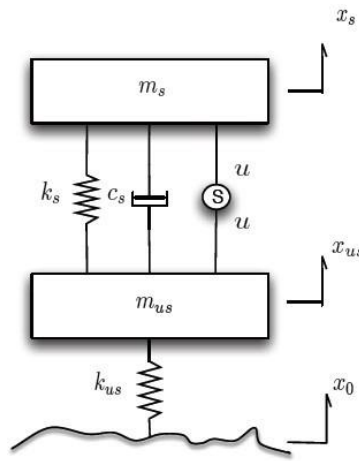


Figure 2.4. Quarter-vehicle suspension model [26].

Longitudinal QV models also consist of a vehicle mass and wheel mass, as shown in Figure 2.5. where w wheel angular velocity, T the motor torque, r wheel radius, M vehicle mass, V vehicle velocity, Fd driving force, and Vw wheel velocity, respectively. These are rigidly connected to each other, and the tyre is rigidly connected to the road.

The vehicle can move on the longitudinal axis and the tyre can rotate on the lateral axis. This model has been used widely to assess wheels' slip and skid control [27],[10], [28].

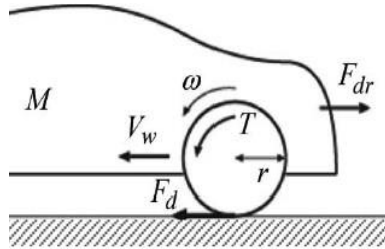


Figure 2.5. Quarter-vehicle longitudinal model [27].

The road is considered flat, therefore suspension dynamics were not relevant to this study. Further, several studies that used the longitudinal QV model did not account for drag force and rolling resistance. As a result, the longitudinal QV model was expected to over-perform as it introduced no losses [10].

2.2 Electric Motor Control System

2.2.1 Background

In modern transportation systems, energy consumption and emissive pollution mainly come about from the use of vehicles. One solution for this problem is the development of EVs, which are designed to minimise pollution; however, there are several on EVs, including limitations on driving range and battery capacity and inefficient charging. As a result, hybrid EVs have been developed to meet the demands of increased driving range and reduced fuel consumption.

Permanent-magnet synchronous motors (PMSMs) are popular for use in hybrid vehicles, as they have better performance, higher efficiency, higher energy density and are smaller than other electrical motors. Additionally, interior permanent-magnet synchronous motors (IPMSMs) provide a wider speed range than surface-magnet synchronous motors due to the robustness of their rotor structure [29]. Because of their advantages, this project concentrated on the high-performance control offered by IPMSM drives.

There are three main control schemes used for high-performance PMSMs: scalar control (v/f), vector control (VC) and direct torque control (DTC). Scalar control—also called open-loop control—has several benefits, such as relative simplicity and reduced cost; however, scalar control is ineffective when it comes to dynamic performance and requires extra damper winding on the rotor side to retain flux linkage in both stator-side and rotor-side synchronising. In short, scalar control adds more complexity to the system.

PMSMs traditionally use VC, which is also called field-oriented control. This control scheme was developed in the 1970s by German researchers for use with induction motors (IM)[30]. In VC, motor torque is controlled indirectly via current control in the rotor reference frame. This necessitates coordinate transformation and the use of a position sensor for the current-control loop. These requirements introduce delays in the system [31], [32]. Additionally, the VC scheme is affected by parameter variations and it limits torque responses by the time constant of stator windings [31].

With the development of high-speed digital signal processors, DTC has become a popular control scheme for EV PMSM drives. In DTC, motor torque and flux linkage are controlled directly and independently. Feedback from torque and flux linkage is processed by an instant estimator. Stator voltage, current vectors and the initial angle of the rotor are used to calculate the flux linkage vector. As such, it is essential to know the initial position and stator resistance. In this scheme, current controllers and mechanical sensors are no longer needed. Since all calculations are performed in the stator reference frame, there is no need for coordinate transformations or continuous data regarding rotor position [32]–[37]. The DTC scheme requires no sensors, reducing cost and increasing reliability. This scheme has several advantages compared to the more traditional VC. These include a simpler control method, no requirement for coordinate transformation, less dependent parameters and fewer controllers [32]-[33].

2.2.2 Common structures of permanent-magnet synchronous motors

PMSMs have several advantages over IMs. For instance, the stator current of an IM consists of many components related to magnetising and production of torque; however, PMSMs only require the production of torque. Due to the absence of a magnetising current, PMSMs achieve higher power factors and greater efficiency than IMs.

Conventional wound-rotor synchronous machines require brushes and slip rings to supply direct current (DC) excitation to the motor. This results in rotor losses and necessitates extra maintenance for the brushes. PMSM was developed to address these drawbacks: a permanent magnet replaces the field coil, slip rings and DC power supply. PMSMs exhibit sinusoidal induced electromagnetic force (EMF) and demand sinusoidal currents for constant torque.

EVs should be able to operate with high efficiency in variable working conditions. they should also act as generators to support traction in boost mode, as drives during traction procedures and should supply power to recover electrodynamics brake. To meet the demands of limited space and high power density and operating efficiency, PMSMs are the preferred variable-speed motor drives for EVs [38].

Figure 2.6 demonstrates two typical PMSM rotor structures: IPMSMs and surface-mounted permanent-magnet synchronous machines (SPMSM). Because ferrite, rare-earth magnets and air are similarly permeable and SPMSMs have large effective air gaps, SPMSMs usually have small levels of stator inductance. As a result, they only function properly in constant-torque operation. Conversely, the small air gaps of IPMSMs have significant effects for armature reactions, which makes them suitable for both constant-torque and field-weakening (FW) operations. Further, because the permanent magnets in IPMSMs are buried inside the rotor, the rotor can be run in high-speed applications.

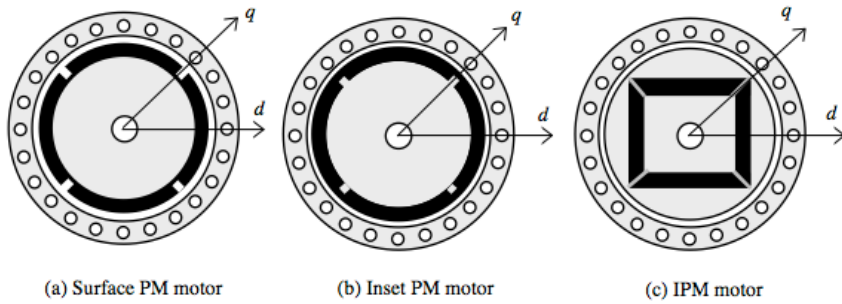


Figure 2.6. Typical rotor cross-sections of permanent-magnet synchronous motors [39].

This project was mainly concerned with IPMSMs, in which the magnets are placed inside the rotor. In IPMSMs, the magnets are placed in cavities bored into the rotor and surrounded by magnetic materials instead of air [40]. Modern magnets are highly resistant to centrifugal forces, making them appropriate for high-speed applications. The main drawback of this approach is placement of the magnets requires advanced processes, increasing the cost.

There are two main types of IPMSM structure [40]: radially placed buried-magnet structures and circular buried-magnet structures. These two different structures are described below.

2.2.2.1 Radially placed buried-magnet structures

In radially placed buried-magnet structures, the magnets are buried around the rotor axis and magnetised (as seen in Figure 2.7). Because of this, these motors have small air gaps, and low armature reactions. Ferrite magnets can be utilised to create high torque density, as the flux density in the air gap is higher than the internal parts of the magnet. Additionally, there is a non-magnetic material surface contact with the rotor in these structures, which makes it possible to avoid magnetic short-circuits; however, the materials are more costly than the alternatives [40].

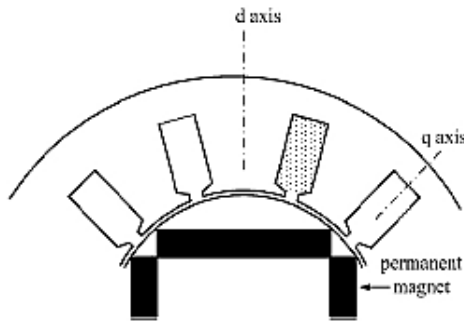


Figure 2.7. Radially placed buried-magnet structure [40].

2.2.2.2 Circular buried-magnet structures

Figure 2.8 shows a circular buried-magnet structure. Unlike radially placed buried-magnet structures, the permanent magnets in circular buried-magnet structures are buried in the rotor and point towards the main axis. As a result, the motor is able to generate induction at the poles independent from the magnetic operating point. As the magnets are also buried in the rotor, these structures can also resist centrifugal forces [40].

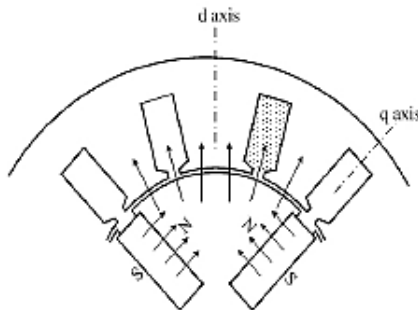


Figure 2.8. Circular buried-magnet structure [40].

2.2.3 Vector control schemes for permanent-magnet synchronous motors

VC was initially proposed for IMs and was only applied to PMSMs later [41]. VC is intended to simulate the magnetic operating conditions of a DC motor, particularly its field-orientation process. In VC drives, it is necessary to know the spatial angular position of the alternating current (AC) motor's rotor flux linkage.

The mathematical modelling of a PMSM is based on a convenient coordinate system that rotates synchronously with the rotor's permanent-magnet axis. The x -axis of this rotor coordinate system is known as the direct axis (d -axis) and the y -axis as the

quadrature axis (q -axis). The magnet flux lies on the d -axis and if the current is controlled in space quadrature with the magnet flux linkage it is aligned with the q -axis [39]. This control strategy is usually written as $i_d = 0$ control. Using this strategy, the reluctance torque becomes zero; therefore, the torque is directly proportional to the stator current on the q -axis (i_q). This makes linear, single-loop torque control possible. Additionally, torque is controlled through control of the stator current.

In 1988, Champenois described two fully digital two-current loop VC structures [42]. The first was based on the typical strategy, which consists of direct control of the phase currents with independent loops. The second structure was developed on the basis that the references and disturbances in the $d-q$ reference frame are constant, which cancels the steady-state current's phase lag and attenuation. Whatever the machine, these equations are simple. Further, it is possible to achieve relatively acceptable performances in terms of dynamic by using the simple $d-q$ loops, EMF feed-forward terms and i_d and i_q as decoupling terms.

In 1998, Takeda and Hirasa proposed a VC structure consisting of a voltage source inverter (VSI) with a rotor position sensor, current sensors and look-up tables for current phase control [43]. The most appropriate current-control method and rotor geometry are determined by simulation and experimentation, taking the saliency of the motor into account. That said, this type of control does not fully utilise the reluctance torque offered by IPMSMs, resulting in a low level of efficiency.

Morimoto performed a study on IPMSMs in 1993. In Morimoto's approach, an armature current vector is actively controlled by controllers based on analysis of load conditions. The purpose of this is to use reluctance torque effectively; it allows a large torque to be produced [44], [45].

The control algorithm for the armature current vector is also described, and the demagnetisation of the permanent magnet and the magnetic saturation both taken into

account. A range of characteristics (e.g., torque, power factor, efficiency, power capability, transient responses, etc.) are verified both by simulations and experimental tests.

The controlled variables in PMSM VC systems are voltage, current and the frequency generated by the controller, all of which are fed to the PMSM through a modulator; therefore, torque is controlled indirectly. PMSM VC drives have good torque response, accurate speed control and full torque at zero speed. Feedback regarding the position of the rotor flux is needed, as are modulators. The current modulator used in VC drive slows down the system response.

Torque control loops have decisive effects on response time and the precision of controls. There are two popular torque and current-control techniques: indirect torque control and DTC.

There are two widely used indirect torque control schemes: open-loop v/f control and VC.

Open-loop v/f control is normally used for fan- and pump-based drives that do not require high performance and fast responses. In VC schemes, two currents— I_d and I_q —are calculated in the rotor reference frame to indirectly represent torque. This procedure is mainly carried out using PWM current control. The conversion between rotor and stator reference frames demands a continuous signal concerning the rotor position.

In 1971, Blaschke presented the first paper on field-oriented VC for IMs . It was later applied to PMSMs. Since then, this technique has been comprehensively developed and occupies a mature position in the industry. Vector-controlled drives are an industrial reality and can be purchased available from several manufacturers, each offering different solutions and performance specifications.

The control of a fully compensated DC machine resembles the earliest VC principles for AC PMSMs. The early strategy involved controlling the current in space

quadrature with the magnetic flux created by the rotor. This results in torque proportional to the product of the current and the flux linkage. To measure the magnetic operating conditions of a DC motor, the VC system requires the spatial angular position of the rotor flux linkage inside the PMSM. In this approach, field orientation is achieved by electronic means rather than through the mechanical commentator and brushes of the DC motor [29].

VC drives have several advantages: they provide good torque response, accurate speed control and full torque at zero speed [29]. Notably, a feedback device is required to obtain a high level of torque response and speed accuracy. There are also several disadvantages to VC drives: they are costly, increase complexity, require modulators that slow down the signal process and motor torque response, and are more electrically complex than DTC drives.

Trajectory control techniques produce reference torque or reference current to control different parameters in constant-torque and FW operations [46]. There are four of these techniques: $i_d = 0$ control, maximum torque-per-ampere (MTPA) control, unity power factor (UPF) control and FW control.

2.2.3.1 $i_d = 0$ control

In this control scheme, i_d is constant (0) at all times. Because the current trajectory on the dq frame is located on the q -axis, this control schema is appropriate for SPMSMs. In SPMSMs, L_d and L_q are equal, meaning they always obtain MTPA when i_d is 0. Conversely, in IPMSMs, torque is proportional to the q -axis current when i_d is 0, but reluctance torque is not fully used. As a result, $i_d = 0$ control is not suitable for IPMSMs [39].

2.2.3.2 Maximum torque-per-ampere control

In 1986, Jahns et al. implemented MTPA control in IPMSMs to improve their efficiency [47]. This control scheme can also minimise the rated power of inverters. On

a normalised i_{dn} and i_{qn} plane, MTPA trajectory is on a tangent to the q -axis (rotor-side) and asymptotic to 45°. When torque is increasing, the reluctance torque term and field-alignment torque term are proportional to the square of current and current [39]. To improve the performance of the MTPA control scheme, it is necessary to control leading angles of the stator current from the q -axis.

2.2.3.3 Unity power factor control

Control of stator current vectors is the key consideration of UPF control. In this scheme, UPF is produced by estimation of stator flux vectors and current vector leading stator flux by 90 degree. Power factor can affect the DC-link current waveform and UPD can also minimise the input current; this means thats an inverter rated for less power or a rectifier can be chosen for current input [29].

2.2.3.4 Field-weakening control

An FW control scheme is used when operating speed surpasses base speed. This scheme boosts the back-EMF of the motor; hence, stator voltage must increase to maintain control over torque and current. However, if the maximum available voltage reaches amplitude of the stator voltage, the torque and current controller will saturate and lose its control capability. Especially in the context of large current references, if I_{ref} exceeds the voltage limit ellipse, the current regulator will lose its control capability first and then cause current regulation to decline to zero. This can be prevented by controlling i_d prior to i_q , allowing current to remain controlled. Jahns suggested that the large error between the reference and measured i_d and i_{q_ref} should be regulated using an error signal to prevent saturation of the current controller.Put another way, motor flux is weakened though i_d control and operation range is extended [39].

Bose proposed an alternative approach for EV drives that involves implementing the stator flux-oriented control [48]. In this scheme, the maximum speed of the drive is limited to 13,750 rpm. The reference and estimated stator flux linkage are compared to

difference controllers; if the reference exceeds actual speed by more than 50 m/s, the current controllers remain saturated and generate a square wave signal. By contrast, PWM current control is employed if the reference is smaller than the actual current. The phase angle of the square wave voltage is generated by torque. Then, by shifting the angle properly, motor flux is reduced, allowing the motor to operate in a constant-power situation. Due to complete saturation of the current controller, the transition from constant-torque to FW is slow.

2.2.4 Direct torque control of permanent-magnet synchronous motors for electric vehicles

Following the introduction of high-performance VC, a new AC motor control was proposed in the 1980s by Takahashi and Depenbrock—it was called DTC [32][41]. Their idea was to control the torque and the stator flux linkage directly, instead of handling and controlling stator current. They did this by regulating inverter switches based on the outputs of hysteresis controllers. The hysteresis controllers process the torque, the stator flux linkage and the stator flux angle position by selecting a proper voltage space vector from a switching table.

In the late 1990s, Rahman et al. published several papers on DTC for PMSMs. One of these papers presented mathematical models for both SPMSMs and IPMSMs and discussed the implementation of DTC in both cases [49]. The proposed scheme was only verified by simulation but not experimental results. They found that torque response was much faster under DTC than under VC.

In [50], [51], some starting methods for synchronous machines (including PMSMs) were proposed that sought to avoid the initial condition problem of the stator flux linkage estimation in DTC. A first-order quasi-integrator was proposed to replace the pure integrator.

It was suggested in [49], [52] that null-voltage space vectors should not be used. Moreover, in a subsequent paper [53], the implementation of two switching tables—one with and one without the null-space voltage vectors—on an IPMSM DTC drive was discussed. Notably, a paper published by other authors [54] did not mention the special effect of the null vectors at all and the switching table with the null-space voltage vectors was used. In [55], additional investigation on the effect of the null vectors in DTC PMSMs was proposed. The authors stated that the idea proposed in [49] was correct only in specific cases, and then a new idea was proposed that if null-voltage space vectors were used rationally, not only could the torque response in DTC PMSMs be improved, but so could the torque and flux linkage ripples.

The controlled variables in DTC PMSM drive systems are the stator flux linkage and torque. Field orientation is achieved without rotor position feedback while the initial rotor position should be known in advance. Motor torque is controlled directly without current control or modulation. The result is a drive with a fast torque response.

DTC schemes are implemented based on the error signal between the reference and the estimated values of torque and stator flux linkage; therefore, direct control of inverter states can reduce the torque and flux linkage errors within the limitation of bands.

By contrast with VC, DTC does not require any coordinate transformation, current regulation or PWM signal generators. Despite its simplicity, DTC produces a fast-response torque control in both steady-state and transient operating conditions. Additionally, this controller is more robust than VC in terms of sensitivity to parameters.

Chapter 3: Mathematical Model for the Electric Vehicle Traction Control System

3.1 Mathematical Modelling of Permanent-Magnet Synchronous Motors

According to the motor model mentioned in chapter 2, in the dq reference frame, the frame rotates synchronously with the rotor. In this frame, the q -axis is directly orthogonal to the d -axis, which is aligned with the direction of the magnets. This frame is commonly used to analyse the dynamic performance of PMSMs [39]. This motor model is made up of the following equations, the parameters for which are listed below:

$$v_q = R i_q + p \lambda_q + \omega \lambda_d \quad (3.1)$$

$$v_d = R i_d + p \lambda_d - \omega \lambda_q \quad (3.2)$$

Here, λ_d and λ_q are the d -axis and q -axis stator flux linkages, which are derived from two additional equations [29]:

$$\lambda_d = L_d i_d + \lambda_f \quad (3.3)$$

$$\lambda_q = L_q i_q \quad (3.4)$$

The general torque equation is as follows:

$$T = \frac{3}{2} P (\lambda_d i_q - \lambda_q i_d) \quad (3.5)$$

Substituting Equations 3.3 and 3.4 into Equation 3.5 in the dq reference frame gives the torque expression, which represents the PMSM [39]:

$$T = \frac{3}{2} P [\lambda_f i_q + (L_d - L_q) i_d i_q] \quad (3.6)$$

The motor dynamics are represented by the following equation:

$$T = T_L + B \omega_R + J p \omega_R \quad (3.7)$$

The parameters for Equations 3.1–3.6 are as follows:

- v_d and v_q are the dq frame stator voltages.
- i_d and i_q are the dq frame stator current.
- L_d and L_q are the dq frame stator inductances.
- ω is the electrical angular velocity (rad/sec).
- J is the moment of inertia.
- P is the number of pole pairs for the motor.
- R is the stator resistance.
- λ_f is the amplitude of the magnet flux linkage.
- ω_R is the rotor speed.

Equation 3.6 combines excitation torque and reluctance torque. The first term, which represents excitation torque, is generated by the interaction of permanent-magnet flux and i_q , and is separate from i_d . The second term, which represents reluctance torque, is proportional to $i_d \times i_q$ and is also proportional to the relationship between L_d and L_q [29].

In SPMSMs, $L_d = L_q$; as a result, the reluctance torque is constant null. Conversely, IPMSMs can achieve higher torque with a greater difference between L_d and L_q when i_d is the same. That said, Equation 3.3 shows that a small negative i_d is required to weaken the magnetic flux of permanent magnets; therefore, i_d only needs a slight reduction to keep the stator current within an acceptable range. Because L_q is greater than L_d in IPMSMs, reluctance torque can compensate for torque decline in FW operations when $i_d < 0$ and reluctance is positive. Because of this, IPMSMs can handle a wider speed range than SPMSMs. When selecting values for motor design, the amplitude of excitation and reluctance torques must be determined [39].

3.2 Direct Torque Control of Permanent-Magnet Synchronous Motors

In DTC, it is essential that flux linkage and electromagnetic torque are controlled directly and independently; therefore, a current-control scheme is not required. Because of this feature, torque response is faster in DTC than in VC. Additionally, the selection of voltage vectors is mainly determined by control performance, such as the speed of torque response and flux linkage. The voltage space vector can be determined by output signals from the hysteresis controller and the angle of the stator flux linkage vector. Because DTC calculations are mainly based on the stationary frame, the need for a position sensor is eliminated. Notably, torque and flux linkage are estimated values in DTC, so estimating errors influence the control scheme's performance [39].

Figure 3.1 shows the stator and rotor flux linkages on two different reference frames: $\alpha\beta$ and dq . $\alpha\beta$ is a stationary reference frame. The α -axis is aligned with phase winding. This frame represents stator currents and DC bus voltage. dq is the rotor reference frame, in which the d -axis is aligned with the rotor flux linkage. Meanwhile, xy is aligned with the stator flux linkage vector.

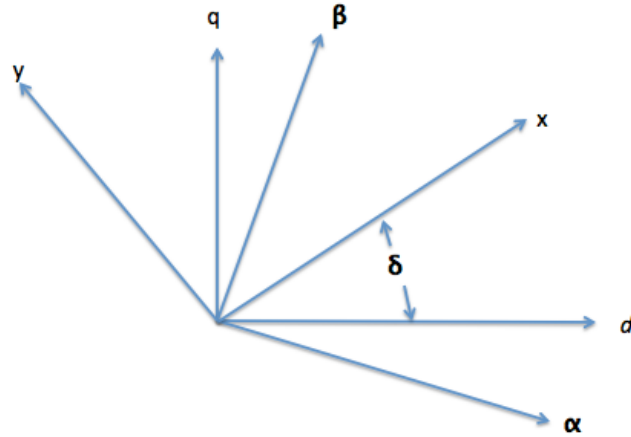


Figure 3.1. The stator and rotor flux linkages directions on different reference frames.

In DTC, the stator flux linkage is estimated by integrating the difference between the input voltage and the voltage drop across the stator resistance [29]:

$$\lambda_D = \int(v_D - i_D R_s)dt \quad (3.8)$$

$$\lambda_Q = \int (v_Q - i_Q R_s) dt \quad (3.9)$$

In the $\alpha\beta$ frame, the stator flux linkage phasor is given as follows [29]:

$$|\lambda_s| = \sqrt{\lambda_D^2 + \lambda_Q^2} \quad (3.10)$$

$$\angle \theta_s = \tan^{-1}(\lambda_Q / \lambda_D) \quad (3.11)$$

The electromagnetic torque is given with the following equation [29]:

$$T_g = \frac{3}{2} P (\lambda_D i_Q - \lambda_Q i_D) \quad (3.12)$$

The torque equation in terms of δ and the generator parameters are given as follows [29]:

$$T_g = \frac{3P|\lambda_s|}{4L_d L_q} (2\lambda_M L_q \sin \delta - |\lambda_s|(L_q - L_d) \sin 2\delta) \quad (3.13)$$

Here, the parameters are defined as follows:

- L_q is quadrature inductance.
- L_d is direct inductance.
- ω is the rotor angle velocity
- T is electromagnetic torque.
- P is the number of pole pairs.
- λ_f is the rotor magnet flux linkage.
- λ_s is the stator magnet flux linkage.

In Equation 3.13, torque is a function of δ when stator flux linkage is a constant.

Conversely, with different values of λ_s , there is a maximum angle for producing maximum torque. This angle can be adjusted by regulating the phase angle of the stator flux linkage; hence, torque can be controlled [39].

3.2.1 Flux linkage and torque with a voltage source inverter

For the stator windings of a three-phase motor normally distributed by a balanced sinusoidal signal, the stator voltage vector v in the $\alpha\beta$ frame can be represented with the following equation [15]:

$$v = \frac{2}{3} (V_a + \alpha V_b + \alpha^2 V_c) \quad (3.14)$$

Where $\alpha = e^{j2\pi/3}$, V_a , V_b and V_c are the values of the phase voltage refer to the ground voltage reference (see Figure 3.2).

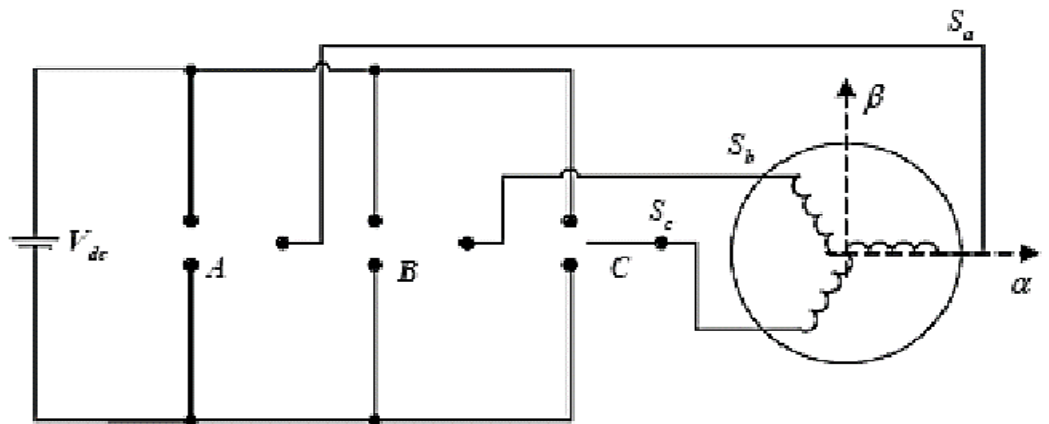


Figure 3.2. Two-level voltage source inverter and a three-phase machine [29].

Figure 3.2 shows an idealised three-phase VSI: pure time delay, forward voltage drop of the power switch, turn-on and turn-off time and other non-linear disturbances are all neglected. Assuming the terminal voltages of A, B and C are controlled by three ideal switches The switching control signals of the three phase terminals are defined as S_a , S_b and S_c , and can be determined only as Boolean variables. As a result, the instantaneous output voltage vector generated by the ideal inverter can be defined as follows [39]:

$$v = \frac{2}{3} V_{dc} (S_a + \alpha S_b + \alpha^2 S_c) \quad (3.15)$$

There are eight voltage vectors for the different combinations of S_a , S_b and S_c , as indicated in Figure 3.3. There are six non-zero voltage space vectors and two zero voltage vectors (V_0 , V_7). Further, for a multi-level inverter, additional voltage space vectors are required to represent all sectors in space.

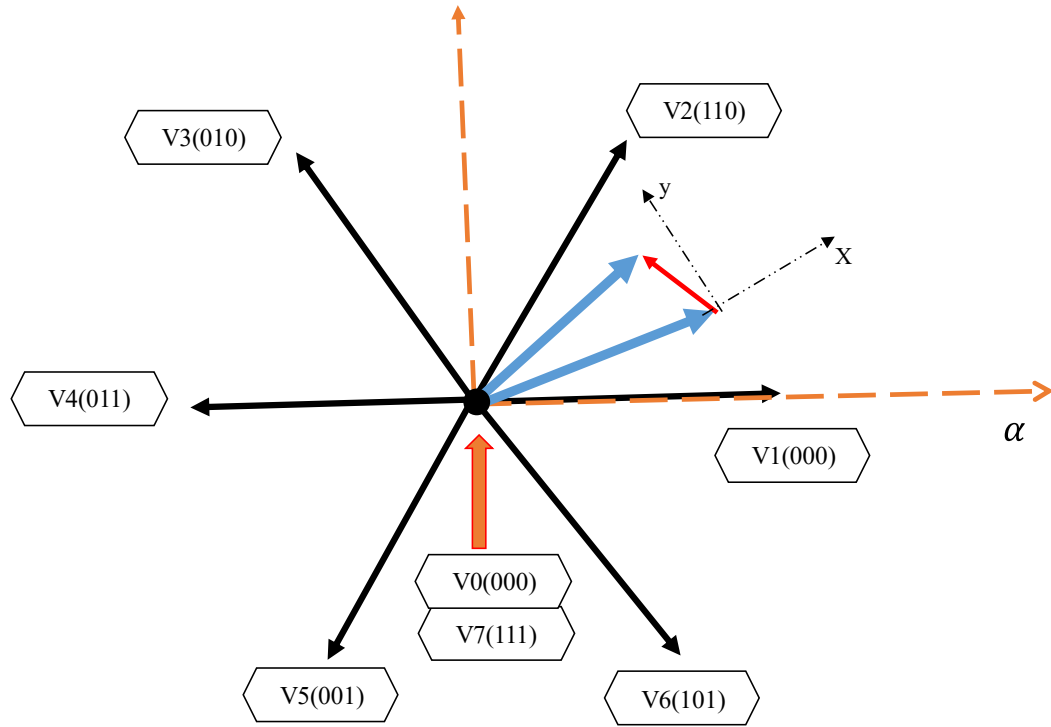


Figure 3.3. Eight voltage space vectors combined by the two-level VSU [39].

In order to represent the relationship between the voltage vector, the current vector and the stator flux linkage vector of an AC machine, an $\alpha\beta$ stationary reference frame was carried out in the course of implementing the voltage space VC scheme for the machine. The following equation was used[39]:

$$v = \frac{d\lambda_s}{dt} + Ri \quad (3.16)$$

Here, R is the stator resistance. The stator flux linkage can be determined by integration of the applied voltage vector minus the voltage drop on the stator resistance [13]:

$$\lambda_s = \int(v - Ri)dt + \lambda_{s0} \quad (3.17)$$

The tips of the stator flux linkage vector (λ_s) move in the same direction as the applied voltage vector, as shown in Figure 3.3. In particular, the magnitude of the stator flux linkage vector moves are determined by the time consumption of the vector and the amplitude of the voltage space vector, the latter of which can be represented as a proportional variable of the inverter's DC bus voltage. The amplitude of the stator flux

linkage vector can be regulated through application of a set of modulated voltage space vectors. The speed at which the stator flux linkage rotates is determined by the sequence of the voltage space vectors; therefore, the stator flux linkage vector can be regulated by applying other appropriate vectors.

To select the voltage vectors (for the purpose of controlling the amplitude of the stator flux linkage), the entire voltage space vector area is divided into six sectors. Each sector represents a space area of 60° . Four voltage vectors must be selected for each space area to minimise the switching frequency. Four voltage vectors can be selected to increase or decrease λ_s . For example, the voltage vectors V2 and V3 increase or decrease λ_s if it is located in region θ_1 and is rotating anticlockwise. Likewise, voltage vectors V5 and V6 are chosen when λ_s is in the same region but rotating clockwise. As such, λ_s can be regulated both in amplitude and direction by selecting the relevant voltage vectors[55].

The two zero voltage vectors, V0 and V7, add more complexity to the control scheme. In accordance with Equation 3.17, λ_s remains in its previous position if zero voltage vectors are applied. This situation is common in IMs because the rotor voltages are zero consistently, which means the stator flux linkage is uniquely determined by the stator voltage. However, for PMSMs, λ_s should remain at its previous position when zero voltage vectors are applied. Additionally, λ_s continues to be supplied by the rotor; as it rotates with the rotor, the induced current generated by the rotor flux linkage eliminates changes in λ_s . According to Rahman et al. and Hu [39], [54], the use of zero voltage vectors reduces the torque ripple of conventional direct torque drives; however, the results collected in this study showed that the reduction in torque ripple by operating the control scheme with zero voltage vectors is relatively small and can be ignored [39].

3.2.2 Direct torque control interior permanent-magnet drive control scheme with look-up table technique

The six voltage space vectors used to control the torque and stator flux linkage are shown in Table 3.1. It is also used for bidirectional operation of the drive, in which case λ and τ are the outputs of the two hysteresis controllers for stator flux linkage and torque, respectively. $\lambda = 1$ indicates the estimated flux linkage is smaller than the reference value, and a flux-increasing vector should be selected. The same principle applies to τ . The region number (shown in Figure 3.4) is represented by $\theta_1 \sim \theta_6$.

Table 3.1

Flux linkage and torque control under direct torque control [39]

		θ					
λ, τ		$\theta(1)$	$\theta(2)$	$\theta(3)$	$\theta(4)$	$\theta(5)$	$\theta(6)$
$\lambda = 1$	$\tau = 1$	V2(110)	V3(010)	V3(010)	V3(010)	V3(010)	V3(010)
	$\tau = 0$	V6(101)	V1(100)	V1(100)	V1(100)	V1(100)	V1(100)
$\lambda = 0$	$\tau = 1$	V3(010)	V4(011)	V4(011)	V4(011)	V4(011)	V4(011)
	$\tau = 0$	V5(001)	V6(101)	V6(101)	V6(101)	V6(101)	V6(101)

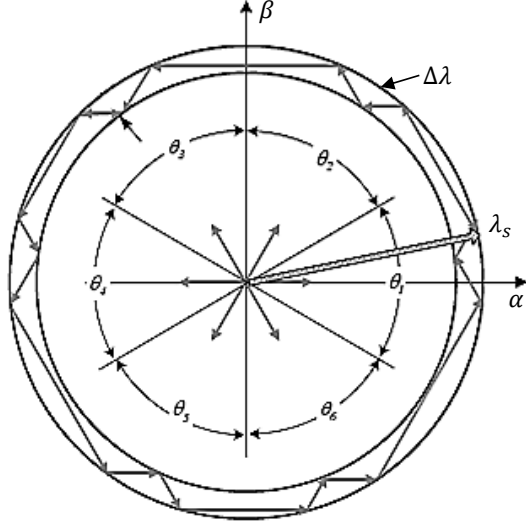


Figure 3.4. Control of the stator flux linkage by applying voltage vectors [39].

3.2.3 Stability criteria

According to previous mathematical analysis, the torque and flux linkage can be regulated by applying proper voltage space vectors. Control of torque is achieved by regulating the angle δ between the stator and rotor flux linkage vectors. By differentiating the torque expression in Equation 3.13, a new equation can be obtained [39]:

$$\frac{dT}{dt} = \frac{3P\lambda_s}{4L_d L_q} [2\lambda_f L_q \cos \delta - 2\lambda_s (L_q - L_d) \cos 2\delta] \dot{\delta} \quad (3.18)$$

The angle between the stator and rotor flux linkage vectors δ for the maximum torque (δ_{max}) can be found from $\frac{dT}{d\delta} = 0$, which produces the following equation [39]:

$$\delta_{max} = \cos^{-1} \left(\frac{a - \sqrt{a^2 + 8\lambda_s^2}}{4\lambda_s} \right) \quad (3.19)$$

Here, a can be determined as follows:

$$a = \frac{\lambda_d L_q}{L_q - L_d} \quad (3.20)$$

To guarantee stable control of torque, the coefficient of Equation 3.18 must be positive.

$$x = \cos \delta \quad (3.21)$$

Because $-\delta_{max} < \delta < \delta_{max}$, a new condition can be obtained:

$$\cos\delta_{max} < x < 1 \quad (3.22)$$

The coefficient of the derivative of torque with respect to time is then calculated as follows [39]:

$$f(x) = \frac{dT}{dt} / \frac{3P\lambda_s}{2L_q L_d} = [\lambda_f L_q x - \lambda_s (L_q - L_d)(2x^2 - 1)]\delta \quad (3.23)$$

Two roots of $f(x) = 0$ can be found with the following [39]:

$$x_1, x_2 = \frac{a \mp \sqrt{a^2 + 8\lambda_s^2}}{4\lambda_s} \quad (3.24)$$

Since one of the roots is $\cos\delta_{max}$, and considering that $L_q > L_d$ leads to the coefficient of the square term to be negative. To guarantee $f(x) > 0$, hold for any x or x_1 must satisfy the following:

$$x_1 > 1 \quad (3.24)$$

As a result, the following equation can be derived from Equation 3.24:

$$\lambda_s < a \quad (3.25)$$

Figure 3.5 shows the variations in $f(x)$ at different stator flux linkage. As long as $x_1 > 1$, torque control is guaranteed; however, the dotted line shows that if $x_1 > 1$, the DTC is not sufficiently stable.

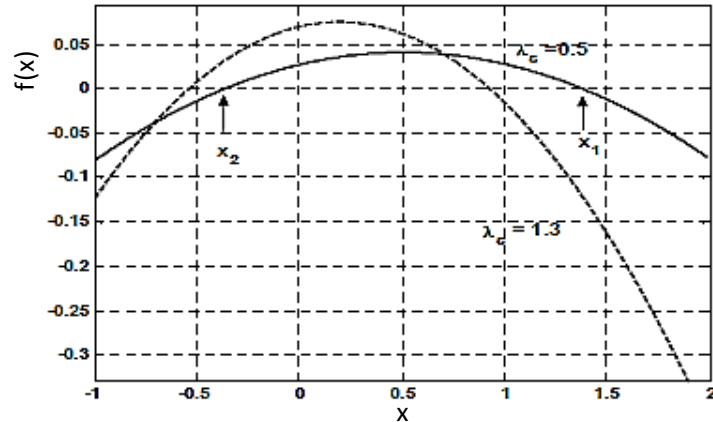


Figure 3.5. Two roots of $f(x) = 0$ with different λ_s [39].

3.2.4 Direct torque control scheme for maximum torque-per-ampere trajectory control

In the DTC scheme, the inputs to the inner loop are the reference torque and the stator flux linkage; therefore, the current-control trajectories in the $d-q$ plane can be mapped on the $T - \lambda_s$ plane. Additionally, the reference flux linkage is determined by the reference torque produced by the speed controller; hence, it is possible to achieve maximum torque-per-ampere trajectory control(MTPA) operation using the DTC. This section discusses the method of trajectory control used in the DTC.

The torque, the amplitude of the stator flux linkage and the angle of the stator flux linkage can be expressed as follows:

$$\begin{cases} \lambda_s = \sqrt{(\lambda_f + L_d i_d)^2 + (L_q i_q)^2} \\ T = \frac{3}{2} P [\lambda_f i_q + (L_d - L_q) i_d i_q] \end{cases} \quad (3.26)$$

$$\delta = \tan^{-1} \left(\frac{L_q}{\lambda_f + L_d i_d} \sqrt{i_d^2 - \frac{\lambda_f}{L_q - L_d} i_d} \right) \quad (3.27)$$

Here, if the current vectors are controlled by the MTPA, it is possible to eliminate the d -axis and determine the relationship between T and λ_s under the trajectory. Unfortunately, this equation is complex and difficult to solve in real-time, so the relationship should be calculated in advance.

3.3 Indirect Torque Control of an Interior Permanent-Magnet Synchronous Motor Drive

For IPMSMs, the voltage and current ratings of the machine and its inverter are the main restrictions on maximum torque capability [33]. Consequently, it is difficult to implement a control scheme to achieve MTPA over the whole speed range and also perform flux weakening control. According to conventional control methods, even when a motor has saliency, there is still unused reluctance torque because the d -axis component of the stator current is regulated to null. To achieve constant and torque operations for

IPMSMs and fulfil the MTPA trajectory, both the d -axis and q -axis current components must be controlled [56].

3.3.1 Stator current trajectories under current control

In the dq reference frame, which rotates synchronously with angular velocity (ω), IPMSMs can be modelled as follows:

$$\begin{bmatrix} v_d \\ v_q \end{bmatrix} = \begin{bmatrix} R + pL_d & -\omega L_q \\ \omega L_d & R + pL_d \end{bmatrix} \begin{bmatrix} i_d \\ i_q \end{bmatrix} + \begin{bmatrix} 0 \\ \omega \lambda_f \end{bmatrix} \quad (3.28)$$

The stator current vector (i) and voltage vector (v) are defined according to the following equations:

$$i = i_d + j i_q \quad (3.29)$$

$$v = v_d + j v_q \quad (3.30)$$

Figure 3.6 presents the steady-state diagram:

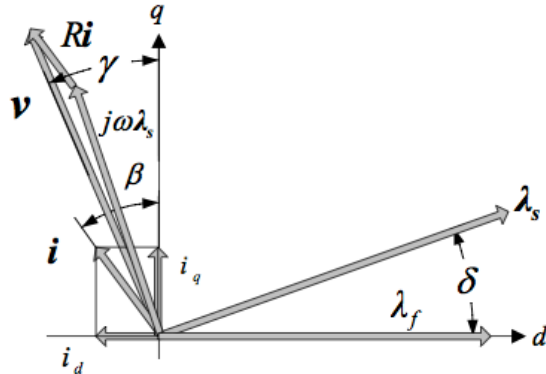


Figure 3.6. Phase diagram of an interior permanent-magnet synchronous motor in a steady state [39].

The leading angles of the stator current and voltage vectors on the q -axis are represented by β and γ , respectively. The dq -axis components for stator can be defined as follows [39]:

$$i_d = -I \sin \beta \quad (3.31)$$

$$i_q = I \cos \beta \quad (3.32)$$

By substituting Equations 3.31 and 3.32 into Equation 3.4, the torque equation becomes as follows [15]:

$$T = \frac{3}{2} \lambda_f I \cos\beta + \frac{3}{2} P(L_q - L_d) I^2 \sin 2\beta \quad (3.33)$$

The first term in Equation 3.33 represents excitation torque and the second term represents reluctance torque. To gain the maximum possible torque at a given amplitude of the stator current, the angle β must be identified. This strategy is the MTPA trajectory [29].

3.3.2 Maximum torque-per-ampere trajectory

Because the current phase angle (β) determines the performance of the control strategy, β must be controlled to obtain the maximum torque and current ratio. This enables a fast transient response and high torque. To get maximum torque, Equation 3.33 can be derived as follows:

$$\frac{dT}{d\beta} = -\frac{3}{2} \lambda_f I \cos\beta + \frac{3}{2} P(L_q - L_d) I^2 \cos 2\beta = 0 \quad (3.34)$$

The MTPA trajectory on the dq coordinate can be derived with the following equation:

$$i_d = \frac{\lambda_f - \sqrt{\lambda_f^2 - 4(L_q - L_d)^2 i_q^2}}{2(L_q - L_d)} = \frac{\lambda_f}{2(L_q - L_d)} - \sqrt{\frac{\lambda_f^2}{4(L_q - L_d)^2} + i_q^2} \quad (3.35)$$

There are two dq components in Equation 3.35; however, i_q can be obtained from the speed loop control system, and the q -axis current is not proportional to torque. This is why the control scheme is referred to as indirect control [39].

3.3.3 Voltage and current constraints trajectory

The maximum stator current and voltage are restricted by the inverter parameter and DC-link voltage ratings, respectively, as long as the IPMSM is fed from an inverter. These constraints can be expressed with the following:

$$I = \sqrt{i_d^2 + i_q^2} \leq I_{max} \quad (3.36)$$

$$V = \sqrt{v_d^2 + v_q^2} \leq V_{max} \quad (3.37)$$

Here, I_{max} and V_{max} are the available maximum current and voltage of the inverter and motor [39].

For simplicity, the analysis of the voltage constraint is based on a steady-state voltage equation, which means that the voltage variables can be replaced with the stator current [29]:

$$\begin{bmatrix} v_d \\ v_q \end{bmatrix} = \begin{bmatrix} R & -\omega L_d \\ \omega L_d & R \end{bmatrix} \begin{bmatrix} i_d \\ i_q \end{bmatrix} + \begin{bmatrix} 0 \\ \omega \lambda_f \end{bmatrix} \quad (3.38)$$

Substituting Equation 3.38 into Equation 3.37 gives the following:

$$V = \sqrt{(Ri_d - \omega L_q i_q)^2 + (Ri_q + \omega L_d i_d + \omega \lambda_f)^2} \leq V_{max} \quad (3.39)$$

If the stator resistance is neglected, Equation 3.39 can be simplified as follows [39]:

$$(L_q i_q)^2 + (L_d i_d + \lambda_f)^2 \leq \left(\frac{V_{max}}{\omega}\right)^2 \quad (3.40)$$

$$i_d = \frac{V_{max}^2}{\omega^2} - (L_q i_q)^2 \quad (3.41)$$

On the $d-q$ plane, the limited voltage trajectory is an ellipse. As shown in Figure 3.7, the size of this ellipse declines when speed increases.

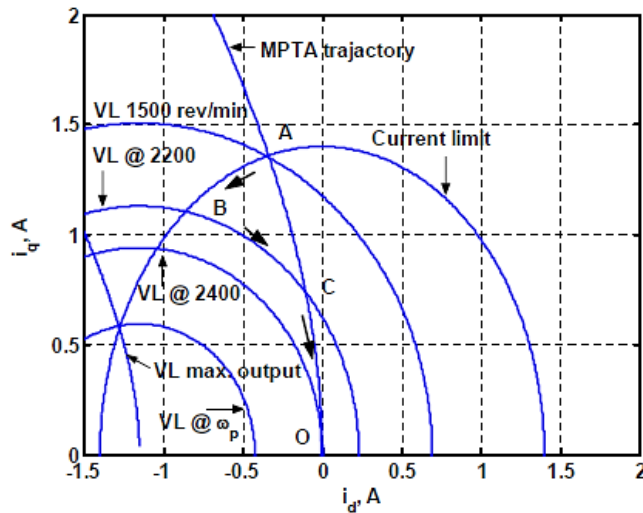


Figure 3.7. Current and voltage constraints trajectory and maximum torque-per-ampere trajectory of interior permanent-magnet motor [39].

3.3.4 Voltage-limited maximum output trajectory

According to [27], a voltage-limited maximum output trajectory was proposed by Morimoto, as represented in the following equations:

$$i_d = -\frac{\lambda_f}{L_d} - \Delta i_d \quad (3.42)$$

$$i_q = \frac{\sqrt{(\frac{V_{max}}{\omega})^2 - (L_d \Delta i_d)^2}}{p L_d} \quad (3.43)$$

$$\Delta i_d = \frac{-p\lambda_f + \sqrt{(p\lambda_f)^2 + 8(p-1)^2(\frac{V_{max}}{\omega})^2}}{4(p-1)L_d} \quad (3.44)$$

In Equations 3.42–3.44, $p = \frac{L_q}{L_d}$.

The current vector trajectory of the voltage-limited maximum output is also shown in Figure 3.7. The rotor speed is set at the minimum speed for maximum output operation under voltage constraints. Below this speed, the trajectory intersects the voltage-limit trajectory at the outside section of the current-limited circle. As a result, the voltage-limited maximum output trajectory must be considered when $\lambda_f / L_d > I_{max}$.

3.3.5 Control mode selection

Based on the MTPA characteristics and limit constraints on current and voltage, Figures 3.8 and 3.9 demonstrate the control trajectories of two different motors suitable for satisfying the above requirements. The selection criteria for the control mode is determined by an analysis of trajectories. For example, the q -axis control current (i_q^*) is given by the external control loop and the current commanded by the d -axis (i_d^*) is determined by Equation 3.35 in MTPA control mode; conversely, it is generated through Equation 3.39 in flux-weakening control mode. All selections are made based on data regarding rotor speed and the load. There are three elements of motor operation determined by base speed (ω_b) and crossover speed (ω_c). The crossover speed is defined

as the value of the rotor speed when the back EMF voltage of unload motor and maximum voltage are identical [29].

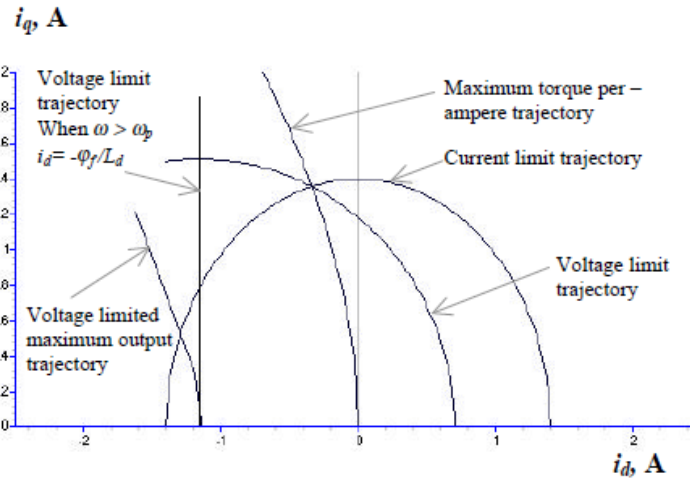


Figure 3.8. Maximum torque-per-ampere, current and voltage limit trajectories on the d-q plane[39].

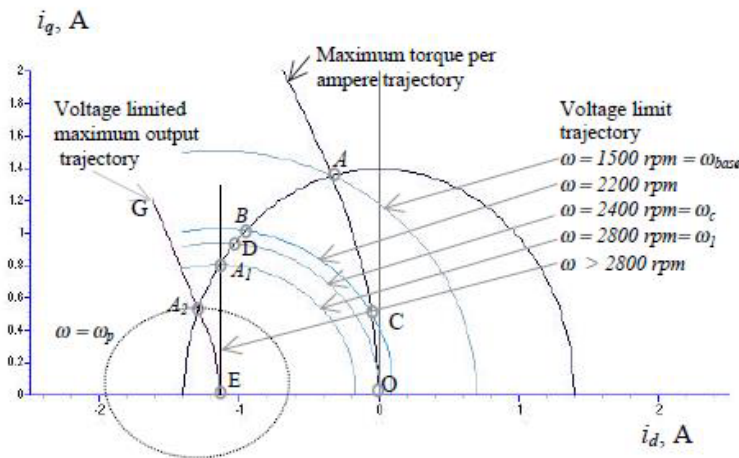


Figure 3.9. Maximum torque-per-ampere, current and voltage limit trajectories on the d-q plane [29].

3.3.5.1 Speed below the base speed

When the rotor is below the base speed, the voltage ellipse is bigger than it is at base speed; therefore, it must satisfy the voltage limitation requirement if the stator current vector is both regulated by the MTPA trajectory and within the current limit. Therefore, the MTPA mode must be used to ensure constant-torque operation.

$$\begin{cases} i_{dmax} = \frac{\lambda_f}{4(L_d - L_q)} - \sqrt{\frac{\lambda_f^2}{16(L_d - L_q)^2} + \frac{I_{max}^2}{2}} \\ i_{qmax} = \sqrt{I_{max}^2 + i_{dmax}^2} \end{cases} \quad (3.45)$$

The maximum values can be used to regulate the speed controller output [39].

3.3.5.2 Speed above crossover speed

The stator flux linkage must be reduced to operate the motor above the crossover speed. Additionally, the voltage limitation requirement ceases to be met when the rotor speed exceeds crossover speed even despite the reduction of flux from the MTPA control. Therefore, the stator current is controlled by the voltage-limited trajectory instead of MTPA. Equations 3.36 and 3.39 determine the current limit and voltage limit. They also determine the d -axis and q -axis limited currents of the control loop for FW operations.

$$i_{dv} = -\frac{\lambda_f L_d}{a} + \frac{1}{a} \sqrt{\lambda_f^2 L_d^2 - ab} \quad (3.46)$$

$$a = L_d^2 - L_q^2, b = I_{max}^2 L_q^2 + \lambda_f^2 - \frac{V_{max}^2}{\omega^2} \quad (3.47)$$

The maximum value of i_{qv} can be determined with the following equation:

$$i_{qv} = \sqrt{I_{max}^2 - i_{dv}^2} \quad (3.48)$$

3.3.5.3 Speed between base speed and crossover speed

The control mode for the rotor speed ($\omega_b < \omega < \omega_c$) is determined based on the load. It can operate near crossover speed with MTPA control when the machine is unloaded. That said, it must be controlled using analysis of the voltage limit trajectory when exceeds the base speed. For instance, when the motor operates at 2200 rpm, the corresponding voltage limit trajectory is shown in Figure 3.9 as the *BCO* area. If the motor is heavily loaded and the current vector follows trajectory, it has to be controlled according to the voltage limit trajectory. Otherwise, MTPA will still be implemented.

Chapter 4: Design and Simulation of a Formula SAE Electric Vehicle Propulsion System

4.1 Introduction

This chapter discusses the development of a propulsion system for an EV for use in the Australasian FSAE competition. It outlines the design methodology for the powertrain system, calculations, and derivation of system parameters; the decision-making procedure used to select different powertrain components; and the design of a custom transmission to optimise the powertrain's performance. Additionally, this chapter discusses the evaluation of the proposed powertrain's performance, which was conducted in the OptimumG simulation environment. It shows that the proposed propulsion system is capable of achieving the performance expected based in line with the FSAE rules and predicted track specifications.

EVs are significantly more efficient than conventional vehicles: electric motors are 95–98 per cent efficient, while internal combustion engines are only 15–20 per cent efficient. Additionally, EVs are quieter and smoother in operation. That said, EVs currently face significant design limitations related to the storage of electricity, which limit their range and necessitate high manufacturing costs [57].

Appropriate parameter-matching of EV powertrains is one of the most efficient ways to improve power transmission, performance and driving range. Extensive research has been performed in terms of calculating and simulating EV powertrains to optimise their performance and identify suitable system parameters [58]. The power characteristics of both motors and transmissions are seldom considered, and the role of transmission ratios in optimising performance is rarely investigated.

This chapter outlines the principles and procedure used in parameter-matching for an EV powertrain, emphasising the interaction between the motor and the transmission. A FSAE EV was used as the basis for this analysis. The FSAE rules limit the power of the EV to 80 kW and the maximum voltage to 600 V [17]. This powertrain system was designed with the aim of improving the vehicle's dynamic performance through optimisation of the electric powertrain through the selection of appropriate parameters. The performance of the proposed system was verified using simulation software to ensure that the performance parameters carefully met the established requirements for powertrain systems as well as the specific EV target design goals.

4.2 Propulsion System Architecture

EV propulsion systems contain four major components: an energy source, an electrical power control unit, a traction motor, and a driveline.

The proposed FSAE EV's accumulator was designed to use lithium cobalt oxide cells as its energy source. A lithium battery was selected due to its long lifespan, high specific energy, and high energy density [59]. A battery management system was required to ensure the safe operation of the energy source. The electrical power control unit consisted of electronic controllers and a power inverter, so that the voltage applied to the traction motors could be adjusted by the control unit based on driver input and load demand. Two PMSMs were employed as traction motors on the basis of their high efficiency, high power density and relatively low cost in comparison to other motors commonly used in EVs [60]. Further, the use of two PMSMs enabled individual wheel control and regenerative braking. This made it possible to simplify the driveline system by removing the differential. Two custom single-gear reduction mechanisms were developed to connect the traction motors and rear wheels. Figure 4.1 shows a schematic of the proposed powertrain configuration.

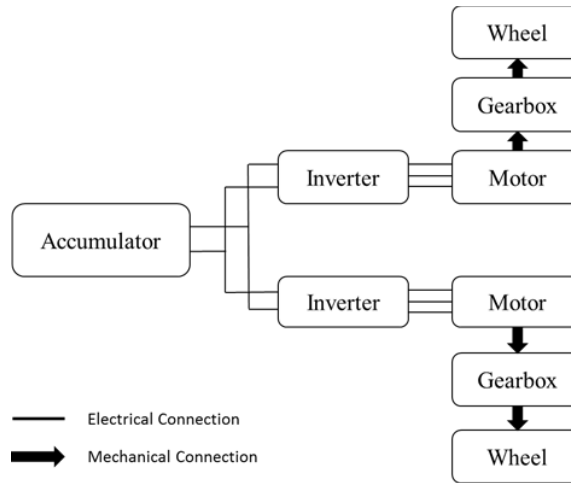


Figure 4.1. Electric vehicle powertrain structure.

4.3 Basic Vehicle Parameters

The dynamic performance of a vehicle is not related to the power characteristics of the powertrain alone, but is also influenced by various resistances (e.g., aerodynamic resistance, acceleration resistance, gradient resistance and rolling resistance). The following equation models the traction force the propulsion system must produce to overcome these resistances:

$$F_t \geq F_f + F_d + F_g + F_i \quad (4.1)$$

Here, F_t is traction force, F_f is rolling resistance, F_d is aerodynamic resistance, F_g is gradient resistance and F_i is acceleration resistance.

$$\frac{T_m i_g i_f \eta_t}{r} = mgf \cos \alpha + \frac{C_D A v^2}{21.15} + mg \sin \alpha + \delta m \frac{d_v}{d_t} \quad (4.2)$$

The values in this equation are defined as follows:

- T_m is traction motor torque.
- i_g is the transmission ratio.
- i_f is the final drive ratio.
- η_t is driveline efficiency.
- r is the wheel radius.
- m is vehicle mass.

- α is the gradient.
- f is the rolling resistance coefficient.
- C_D is the aerodynamic resistance coefficient.
- A is the frontal area.
- v is vehicle velocity.
- δ is the rotational inertia coefficient.

Basic parameters for the EV were estimated based on the specifications of the 2015 UTAS FSAE vehicle. These parameters are outlined in Table 4.1.

Table 4.1

Basic vehicle parameters of 2015 UTAS FSAE vehicle

Parameter	Value
Mass (with driver)	335 kg
Aerodynamic resistance coefficient	0.6
Aerodynamic efficiency	0.083
Frontal area	1.2 m ²
Drivetrain efficiency	90%
Tire rolling radius	0.229
Air density	1.23 kg/m ³
Tire rolling drag coefficient	0.05
Wheelbase	1591 mm

Key performance indicators were set that represented the design goals regarding the EV's dynamic performance (see Table 4.1).

Table 4.2

Key performance indicators of the vehicle

Key performance indicators	Value
Maximum speed	120 km/h
0–75 m acceleration time	4.5 s
Endurance driving range	24 km
Maximum longitudinal acceleration	7.2 m/s ²
Maximum climbable gradient	30°

4.4 Propulsion System Design Methodology

4.4.1 Electric motor drive system

The selection of tractive motors with appropriate parameters was crucial to the whole process. If inappropriate parameters were selected, the motors would operate in either an overloaded or underloaded state. This could lead to inefficient operation of the motors, wasted battery capacity and even the possibility of motor failure [61]. Continuous power, peak power and peak torque were the primary parameters relevant to the traction motor selection. It was expected that the vehicle would run below its maximum speed for the majority of an FSAE race; however, an appropriate power margin was required to support frequent acceleration. The vehicle speed was proportional to the motor output power. As a result, it was possible to initially determine the maximum rated power based on the maximum vehicle speed (V_{max})

$$P_c \geq \frac{1}{\eta} \left(\frac{mgf}{3600} V_{max} + \frac{C_d A}{76140} V_{max}^3 \right) \quad (4.3)$$

Here, P_c is continuous power and η is transmission efficiency.

The operating conditions of racing vehicles demand high acceleration capability and relatively low climbing performance. Therefore, the peak motor power needed to meet power demands for a short time.

$$P_{max1} \geq \frac{1}{\eta} \left(\frac{mgf \cos \alpha}{3600} V_a + \frac{mg \sin \alpha}{3600} V_a + \frac{C_d A}{76140} V_a^3 \right) \quad (4.4)$$

In this equation, α_{max} is the maximum climbable gradient and V_a is vehicle speed.

Assuming the transmission ratio is known, the maximum torque demand in identical working conditions can be calculated with the following equation:

$$T_{max} \geq \frac{r}{\eta i_f} \left(mgf \cos \alpha_{max} + mg \sin \alpha_{max} + \frac{C_d A}{21.15} V_a^2 \right) \quad (4.5)$$

Here, r is the tire rolling radius and i_f is the transmission ratio.

It was also necessary to calculate the peak power required to accelerate the vehicle to the desired speed within the proposed time interval. The peak power was calculated using the following equation:

$$P_{max2} = \frac{1}{t\eta} \left(m\delta \frac{V_m^2}{3600*2\sqrt{t}} + mgf \frac{V_m}{1.5*3600} + \frac{C_d A V_m^3}{21.15*2.5*3600} t \right) \quad (4.6)$$

Here, t is acceleration time and V_m is maximum speed.

According to the operational characteristics of the motor, high torque can be attained on a constant basis at lower rpm ranges, while peak power can be achieved at higher rpm ranges. The efficiency of the electric motor was dependent on the motor's rpm and output torque; hence, it needed to be optimised for maximum efficiency within normal rpm and torque ranges.

The parameters derived using Equations 4.3–4.6 are shown in Table 4.3.

Table 4.3

Electric motor parameters

Parameter	Value
Continuous power	25–40 kW
Peak power	80 kW
Rated speed	2500–3000 rpm
Peak torque	140 Nm

Several features are required to utilise certain electric motors for propulsion systems in racing applications [62]. These include:

- high torque from standstill
- high power density for acceleration
- overload capability in the high-speed region
- high efficiency over wide speed and torque ranges
- regenerative braking capability
- minimal torque ripple
- temperature management
- high reliability and robustness.

PMSMs were the motors most suitable for meeting these requirements and the specifications outlined in Table 4.3. This was due to their high power density, reduced rotor loss and compact packaging.

To reduce complexity, the high-voltage energy storage system was directly connected to the inverter motor drive without a bidirectional DC/DC converter (see Figure 4.). Semiconductors, including insulated-gate bipolar transistors, were used to supply voltage to the traction motor. The voltage rating, current rating, power rating, and switching frequency of the power inverter needed to be compatible with the rating of the energy storage system and motor. Additionally, the four-quadrant operation was required to facilitate traction motor's regenerative braking function.

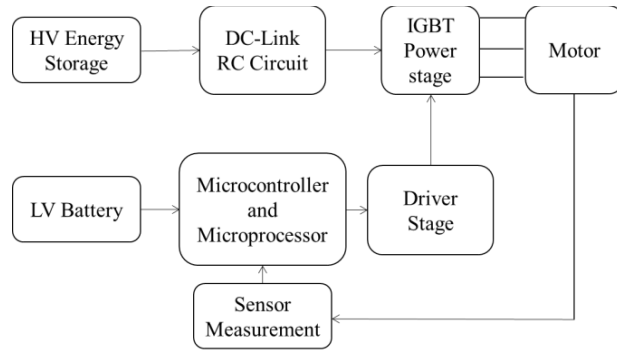


Figure 4.2. Motor drive system.

4.4.2 Transmission

For optimal performance, electric motors should be operated in their high-efficiency range. This can only be achieved with a variable-transmission drive; however, the selected motor featured a constant torque curve, which eliminated the need for a variable-transmission drive.

In fixed-transmission drives, the transmission can be designed to optimise motor performance by ensuring that the motor operates in its highest efficiency range most of the time. That is, at the average velocity of any given track, the motor should operate in its highest efficiency region—96 per cent efficiency, in this case.

The range of transmission ratios (i) at which an EV can be calculated using the following equations [63]:

$$\frac{1}{\eta_t} \frac{mg(f\cos\alpha + \sin\alpha)r}{T_{max}} \leq i \leq 0.377r \frac{n_{max}}{v_{max}} \quad (4.7)$$

$$1.32 \leq i \leq 4.32 \quad (4.8)$$

With the smaller gear ratio, the vehicle would be torque-limited. With a gear ratio of 1.32, the peak torque at each wheel would only be 211.2 Nm, which would not be sufficiently competitive. Lower torque translates to lower acceleration and higher lap times.

With the highest gear ratio of 4.32, a top of speed of 120 km/h can be reached with a peak torque of 691.2 Nm. As a result, this gear ratio was most beneficial in terms

of vehicle performance. As FSAE tracks have few straight sections, it was unlikely that the EV would reach a top speed of 120 km/h.

Once a transmission ratio had been calculated that would optimise performance, the next step of the design process was to evaluate different methods for achieving the necessary reductions. For their transmission systems, FSAE vehicles tend to use stepped-gear transmissions, chain reductions, and differentials. Chain drive systems are frequently used in conjunction with internal combustion engines; conversely, electric motors are coupled with planetary gears, spur gears, belt reductions and chain-and-sprocket reductions depending on the preference of each team and the availability of resources.

A decision matrix was created to ensure that an informed decision was reached regarding the most suitable transmission option (see Table .4). Each factor was weighted based on the importance of each criterion and then scored.

Table 4.4

Weighted decision matrix for selection of reduction mechanism

Design Criteria	Weight factor (/5)	Planetary gear (/5)	Spur gear (/5)	Chain drive (/5)	Toothed belt drive (/5)
Low weight	5	4	4	4	3
Low volume	5	5	5	2	2
In-house expertise	3	3	3	5	3
Low cost	5	1	3	5	3
Pre-tensioning	3	3	3	1	1
Lubrication	3	1	1	2	3
Efficiency	4	4	4	1	1
Manufacturability	5	3	4	4	3
Total points	33	24	27	24	19

A brief explanation of each design criterion in the decision matrix follows:

- Low weight is critical for race cars. Reduced weight translates to better performance as less force is required to overcome inertial forces.
- Volume was an important consideration due to packaging issues. The smaller the component, the easier it is to fit it in the car alongside the other components.
- In-house expertise refers to the available knowledge base. This can include team experience, workshop staff, faculty advisers and the availability of technical advice for design and manufacture.
- Low cost was critical as the team operated on a limited budget.
- Pre-tensioning was important as the introduction of tensioning would complicate the design.
- Lubrication was significant because components that require lubrication are harder to maintain and add to the complexity of the design.
- High efficiency was preferred as this minimises losses in the transmission, which translates to better performance and more points at the competition (especially in the endurance event).
- Manufacturability was an important consideration. The ability to manufacture components using facilities available at the University minimises costs and improves student learning experiences.

As shown in Table 4.4, spur gear reductions received the most points in the decision matrix. This indicated that spur gears were the most suitable reduction mechanism. There were several benefits to using a spur gear reduction system. These included:

- comparable weight to other systems, with potential for weight reduction by using lower safety factors for design and lightweight materials

- by far the most compact design, with very low volume, making it easier to package
- high efficiency in transferring torque to the wheels, thus minimising losses
- a straightforward design that has been widely implemented
- the availability of low-cost gears, which significantly reduced the cost of the gearbox
- most other components could be manufactured in-house.

A set of helical gears with a reduction ratio of 4.267 were sourced from a mass-produced passenger vehicle. The average speed of an FSAE track is roughly 50 km/h; for the selected gear ratio of 4.267, this translated to 2471 rpm for the motor, which was in the middle of the 96 per cent efficiency region for the selected motor.

4.4.3 Gearbox design

The choice of gears simplified the process of designing the gearbox. Since the gears were proven to be reliable and durable and had the capacity to handle the torque and power produced by the electric motors, it was not necessary to perform a detailed finite element analysis of the gear set.

The propulsion system was integrated into the EV as shown in Figure 4..

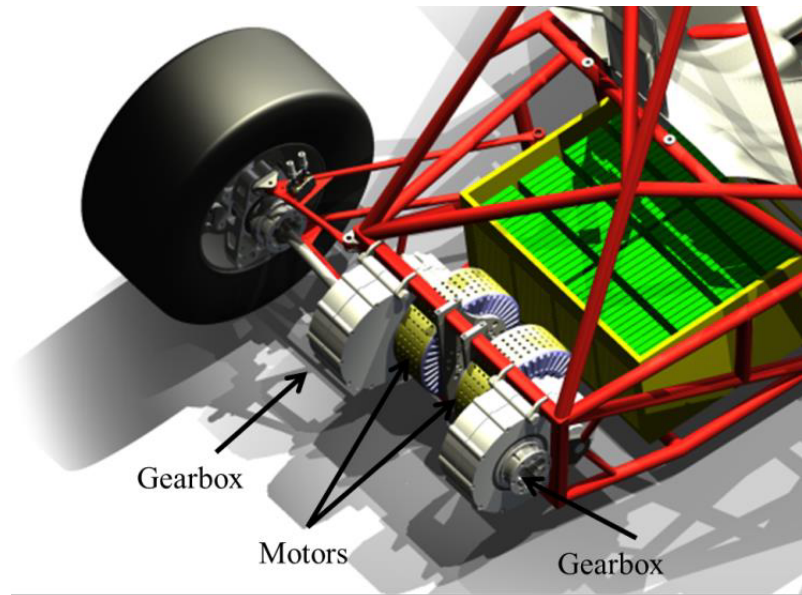


Figure 4.3. Overview of propulsion system.

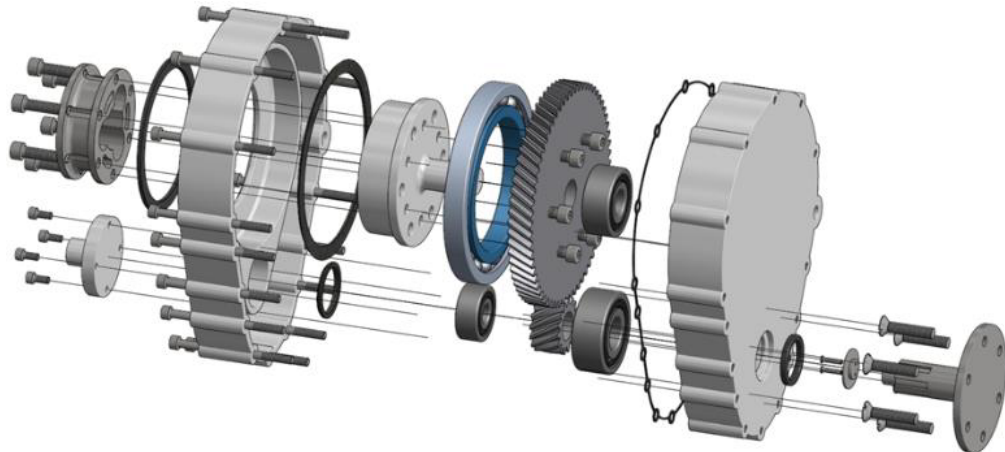


Figure 4.4. Proposed gearbox design.

The weight of the proposed gearbox was less than 9 kg with room for further optimisation. Most components were able to be manufactured in-house. Figure 4.4 shows the results of a sample finite element analysis. This analysis—based on the motor’s peak load output—provided safety factors for critical components of the gearbox (see Table 4.3).

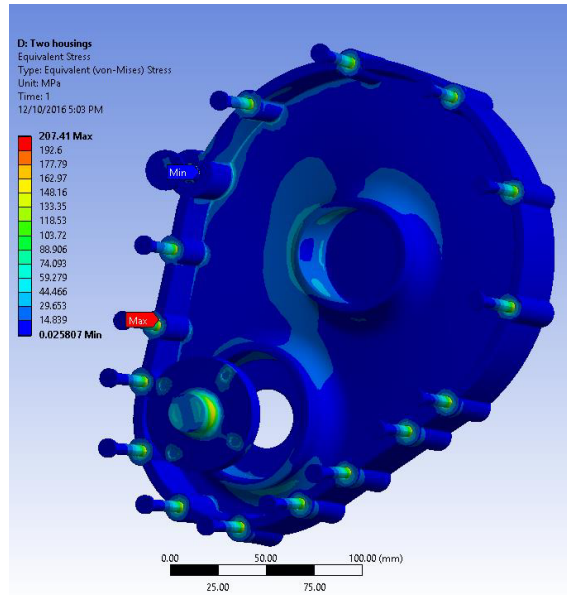


Figure 4.5. Finite element analysis of the gearbox.

Table 4.3

Safety factors of all analysed gearbox components

Component	Safety factor
Gearbox housing (wheel side)	4.3093
Gearbox housing (motor side)	4.5400
Shaft for pinion gear	0.2043*
Shaft for output gear	3.3656
Gearbox housing assembly (bolts)	1.2053
Gearbox housing assembly (housings)	~ 3.000

Note: * This result was generated without surface-hardening the spline.

4.5 Simulation Analysis of the Powertrain

The design was simulated and verified using Vehicle Dynamics Solutions. OptimumG is an international vehicle dynamics consultant group that works with automotive companies and motorsports teams to enhance their understanding of vehicle dynamics [64]. The track used for the Formula Student Germany 2011 competition was used to simulate the powertrain (see Figures 4.5–4.8).

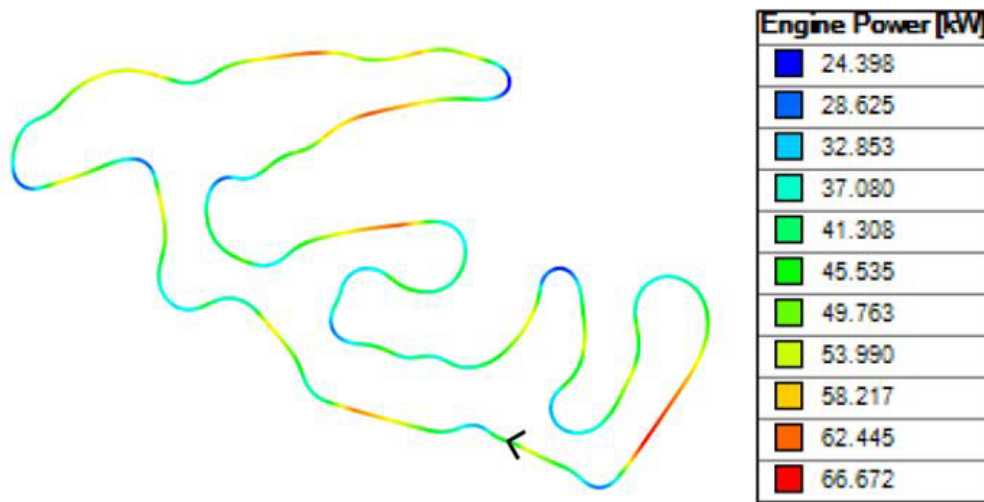


Figure 4.6. Contour plot of on-track power consumption.

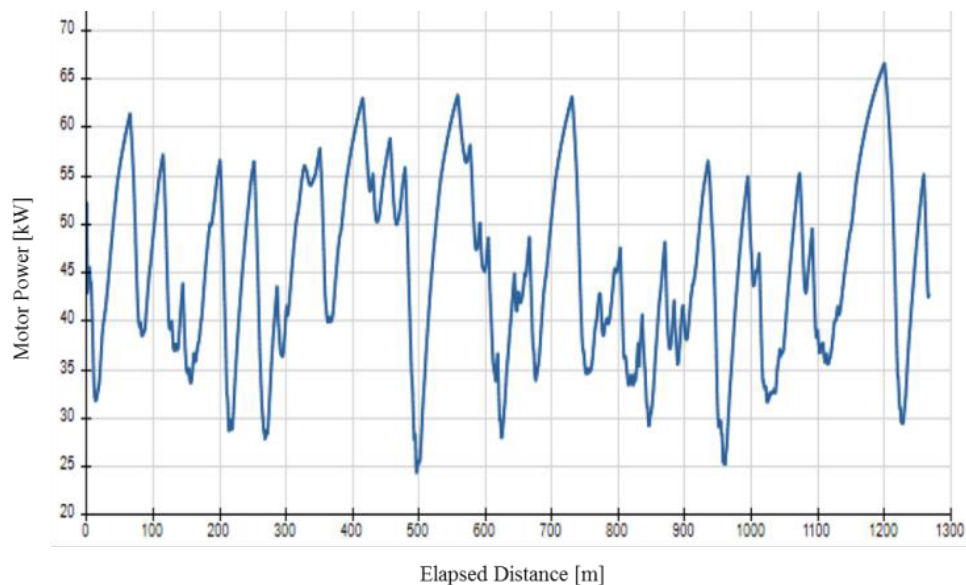


Figure 4.7. On-track power consumption as a function of elapsed distance.

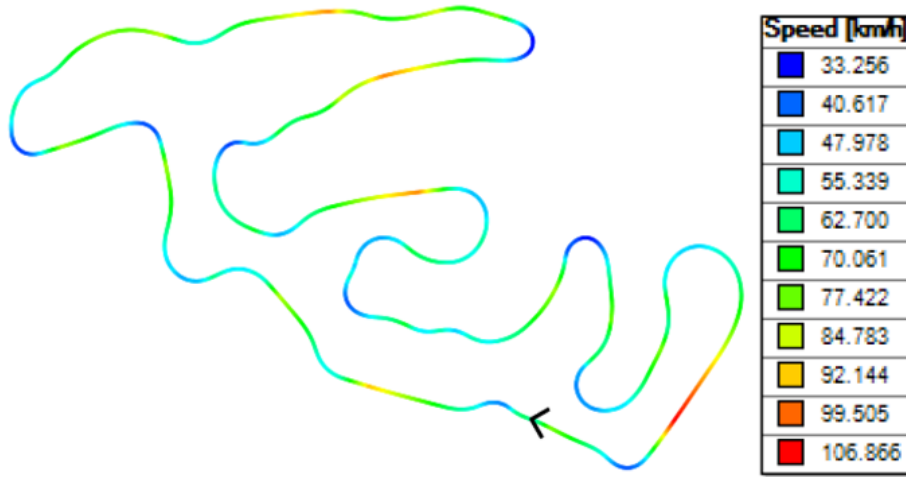


Figure 4.8. On-track speed variation.

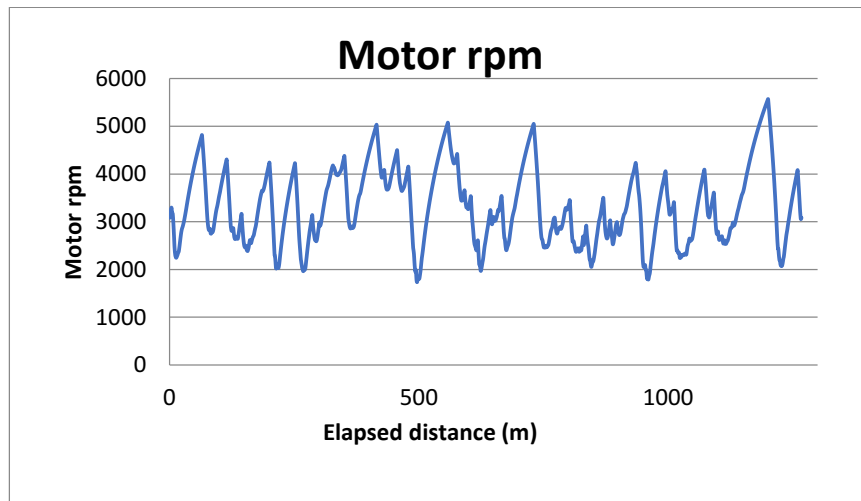


Figure 4.9. Variations in on-track rpm with elapsed distance.

As demonstrated in Figures 4.5 and 4.6, the maximum power produced by the vehicle on the given track was 66.672 kW—below the 80 kW limit. This ensured that the proposed design adhered to FSAE rules and would do so during the competition.

The maximum speed of the vehicle was 106.9 km/h, which was below the intended maximum speed of 120 km/h (see Figure 4.5). This was due to the limited straight sections of road on the track and the lack of gearing; because of these factors, the car did not have sufficient time to accelerate to higher speeds. Regardless, as the track was typical of FSAE tracks, this result indicated that the proposed design would perform relatively well.

Figure 4.6 shows the motor rpm variations along the track. The selected motor had a peak of 6000 rpm, and its most efficient rpm range was between 2500–3500. The simulation indicated that the average rpm of the motor would be in its highest efficiency range; thus, motor performance would be optimal. This showed that the designed transmission was effective at optimising motor performance for this application.

4.6 Conclusion

This chapter discussed the proposed propulsion system. It also presented the parameter-matching procedure for the EV powertrain, emphasising the interaction between the motor and the transmission. The EV was designed with the aim of improving the vehicle's dynamic performance through optimisation of the electric powertrain through the selection of appropriate parameters. This chapter presented the results from the evaluation of different transmission options, a process that emphasised the key criteria. The evaluation showed that a gearbox with a reduction ratio of 4.32 was the most appropriate reduction mechanism. In line with this finding, the detailed design of the custom gearbox was also presented.

Next, this chapter discussed the verification of the powertrain system and its computed values using simulation analysis. The analysis indicated that the selected components would perform relatively well. The maximum power produced by the EV on the example track met FSAE regulations. The EV's maximum speed on the track was below the designed speed for reasons that were discussed. The simulation also showed that the motor would operate in the most efficient rpm range for the majority of the race; thus, it confirmed that the design of a transmission was an effective way to optimise performance.

Given the assumptions made regarding basic vehicle parameters, further study is required to derive precise values that closely represent a FSAE EV. This would improve the accuracy of the simulations. Further data will also be obtained by on-track testing of

the proposed vehicle following manufacture. It will then be possible to compare the results of this testing with those of the simulation.

Chapter 5: Simulation Study of the Traction Control System

5.1 Simulation Studies of the Direct Torque Control Interior Permanent-Magnet Drive

The structure of the proposed DTC drive is shown in Figure 5.1. The hysteresis controllers for torque and flux were designed to calculate the error signal between the reference and estimated torque and flux. The drive is able to identify the output as either high (1) or low (0) depending on whether the estimated values or reference values are higher. Because the switching points are arbitrary, the switching frequency of DTC is not constant. It varies with different bandwidths of the hysteresis controller, load torque and rotor speed. An appropriate stator voltage vector can be selected using the switching logic function, which satisfies both the torque and flux comparator outputs [39].

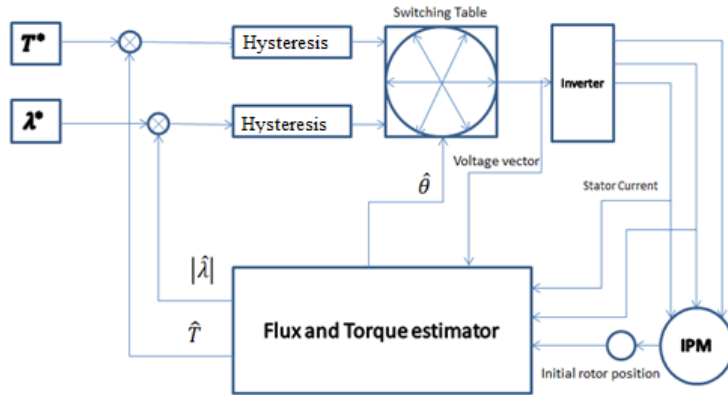


Figure 5.1. Block diagram of the look-up table for the direct torque controlled interior permanent-magnet drive.

The flux and torque estimators are essential components of the DTC drive. The flux can be estimated by operating an integrator (see Figure 5.1). The flux estimator can be written as follows for a digitised controller [39], and index k is reference value:

$$\begin{cases} \lambda_\alpha(k) = \lambda_\alpha(k-1) + (v_\alpha(k-1) - R i_\alpha(k-1)) T_s \\ \lambda_\beta(k) = \lambda_\beta(k-1) + (v_\beta(k-1) - R i_\beta(k-1)) T_s \end{cases} \quad (5.1)$$

$$\begin{cases} \lambda_s(k) = \sqrt{\lambda_\alpha^2(k) + \lambda_\beta^2(k)} \\ \theta_s(k) = \alpha \tan \left(\frac{\lambda_\alpha(k)}{\lambda_\beta(k)} \right) \end{cases} \quad (5.2)$$

The electromagnetic torque in the $\alpha\beta$ reference frame can be represented as follows (see Figure 5.2):

$$T_g = \frac{3}{2} P (\lambda_D i_Q - \lambda_Q i_D) \quad (5.3)$$

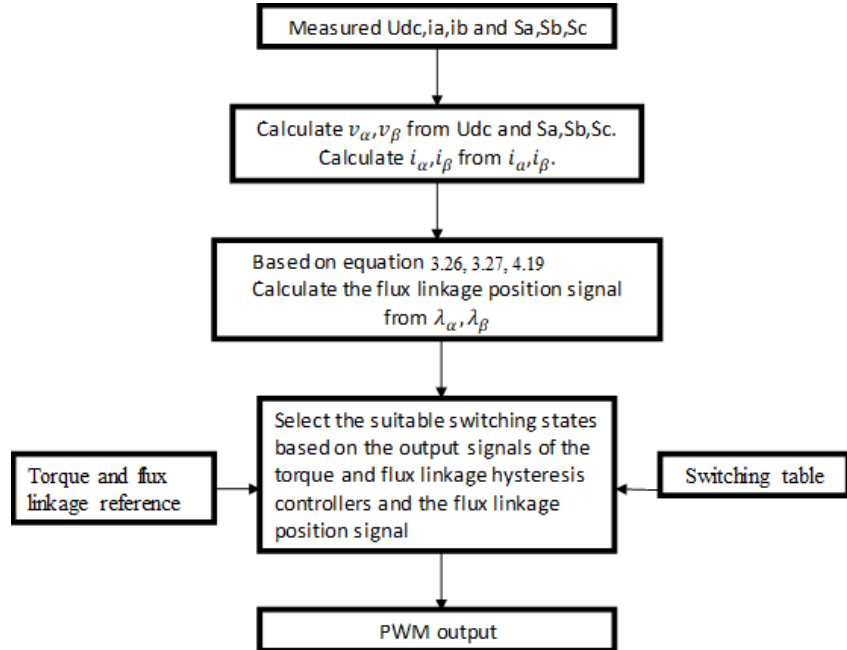


Figure 5.2. Flow chart for the conventional permanent-magnet synchronous motor, direct torque control system.

The output of the speed PI controller gives the torque reference and the inputs of the hysteresis controllers are the errors of the torque and flux linkage. The proper voltage space vector is selected from the switching table based on the position signal of the estimated stator flux linkage vector and the outputs of the two torque and flux linkage hysteresis controllers. Thus, the amplitude, rotating speed and direction of the stator flux linkage vector can be controlled and a fast torque response achieved [39].

The voltage space vectors used in Equation 3.26 can be calculated with Equation 3.14 and 3.15. The $\alpha\beta$ components of the six available non-zero voltage space vectors are shown in Table 5.1 and the parameters for the machine are shown in Table 5.2.

Table 5.1

The $\alpha\beta$ components of the non-zero voltage vectors [39]

	V1	V2	V3	V4	V5	V6
v_α	$\frac{2}{3}v_{DC}$	$\frac{1}{3}v_{DC}$	$-\frac{1}{3}v_{DC}$	$-\frac{2}{3}v_{DC}$	$-\frac{1}{3}v_{DC}$	$\frac{1}{3}v_{DC}$
v_β	0	$\frac{\sqrt{3}}{3}v_{DC}$	$\frac{\sqrt{3}}{3}v_{DC}$	0	$-\frac{\sqrt{3}}{3}v_{DC}$	$\frac{\sqrt{3}}{3}v_{DC}$

Table 5.2

Parameters in direct torque control interior permanent-magnet drive modelling

Parameter	Value
Simulation step	$50 \mu s$
Direct current bus voltage	340 V
Sampling interval of hysteresis controllers	$65 \mu s$
Hysteresis bandwidth of torque controllers	0.00 Nm
Hysteresis bandwidth of flux controllers	0.00 Wb
Sampling interval of speed loop	$2 \mu s$
K_P for speed controller	0.4 Nm*Sec/rad
K_i for speed controller	6 Nm*Sec/rad

Figure 5.3 shows the modelling results, including the stator current, torque and speed. Each was set at 3 Nm load torque with a sampling time of $75 \mu s$. The reference speed was set as a variable-amplitude step function.

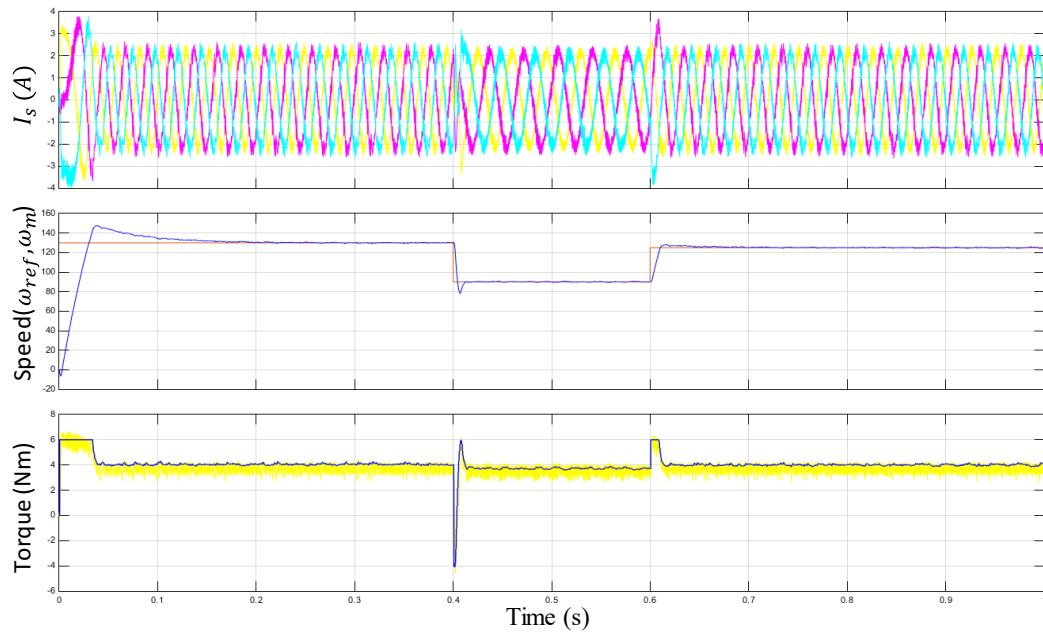


Figure 5.3. Stator current, motor speed and torque response.

Table 5.3

Step functions for load torque

Time (s)	Speed (rpm)
0	130
0.4	90
0.6	125

As shown in Figure 5.3, there were relatively large ripples in the torque—almost 14 per cent of the rated torque, which is too high for an EV motor. Due to some features of the PI controllers, the torque spiked when the load torque changed; however, the transient time was less than 0.02 s and the overshoot of the speed response was small and minimised. The period of that spike was the time it took for the PI controllers to reach a steady state. These large ripples resulted in high current distortion and did not satisfy industrial requirements.

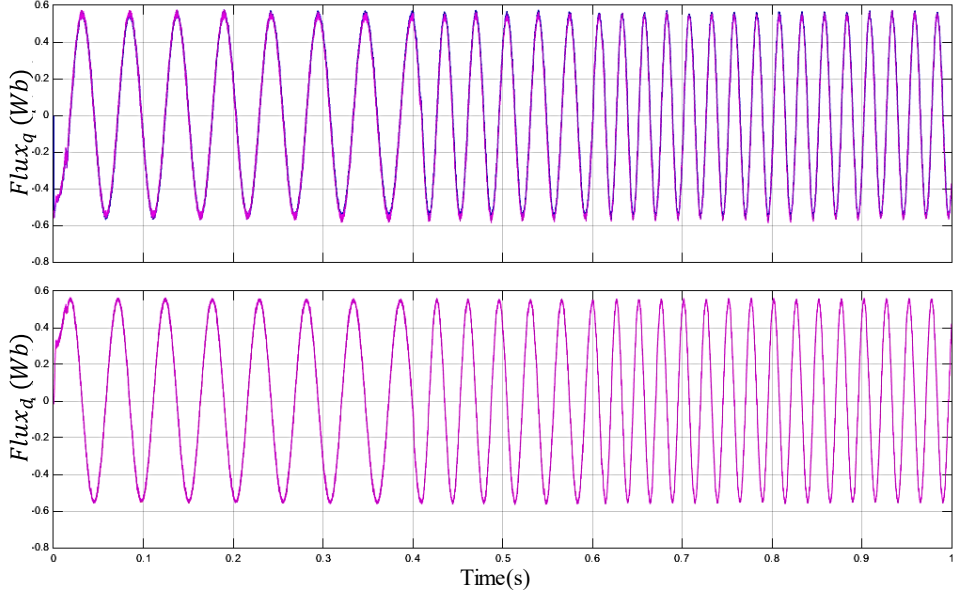


Figure 5.4. Flux linkage for d and q components.

Figure 5.5 plots the flux linkage trajectory from the simulation. A circular flux linkage was observed in constant-torque operation. SVM DTC can produce a smooth stator flux linkage that ensures the rotor rotates in a stable magnetic field; thus, the output of the motor would also be smooth.

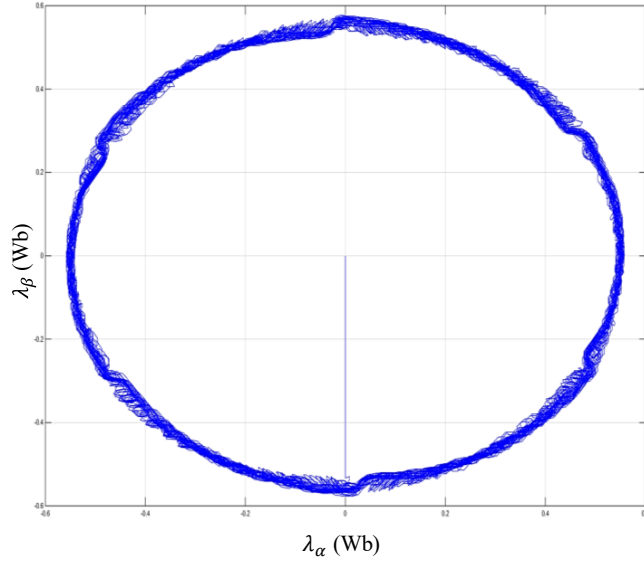


Figure 5.5. Locus of the stator flux linkage under direct torque control scheme.

5.2 Basic Problems Associated with Direct Torque Control for Permanent-Magnet Synchronous Motors and Improvements

The conventional DTC strategy is typically implemented by selecting a proper voltage space vector from an optimised switching table based on two output signals—from the torque and flux linkage hysteresis controllers—and the flux linkage position signal. The inputs of the hysteresis controllers are the error of the reference and the estimated torque and stator flux linkage. The stator flux linkage is estimated by the estimated motor terminal variables (voltage and current), and the torque is calculated from the estimated flux linkage and the measured current.

5.2.1 Stator resistance variation

It is essential to estimate both torque and flux linkage to process the control signal in DTC; hence, according to Equations 3.31 and 3.32, errors in torque and flux estimation can be caused by any variable value of actual stator resistance and controller resistance. This issue reduces the control scheme's performance. Also, a stator resistance estimator is recommended for DTC drives. There are very few options that can be implemented in IPMSMs and there have been few experimental demonstrations [39].

5.2.2 Non-linear effects by inverter characteristic

Dead time and forward voltage drop are counted as non-linear inverter effects. The high voltage applied to the motor terminal renders the voltage distortion caused by this issue negligible [15]; however, these non-linear effects can cause significant errors in voltage when the machine operates at low speeds. They also cause significant errors in voltage and torque estimation.

5.2.3 Offset errors in measurement of voltage and current

Offset errors are common in electrical measurements, including those performed by voltage sensors and current sensors. Theoretically, a small error in measured signals can drive the output of the integrator to either infinity or zero in the steady state. There is

a solution reported in [65]: the integrator can be replaced by a low pass filter, which removes DC items in output signals.

5.2.4 Initial rotor position estimation

The initial rotor position is required to smoothly start the motor. A high-frequency voltage injection has been developed to estimate this initial position [66]. The estimation of this error has been proved to be less than five mechanical degrees, which is sufficient for PMSMs to operate under DTC schemes.

For the speed control loop, a speed signal is required. A speed estimation scheme based on estimated stator and rotor flux linkages can be used to provide signals for speed controllers [39].

5.2.5 Unacceptable ripples in torque and flux linkage

In conventional DTCs, ripples in torque and flux still occur even when the controllers work at high sampling frequencies. These ripples lead to rough operation and fatigue failures in the shaft. Further, there are limitations of increasing sample rate within software and also leads to a high distortion in steady state stator current. Output filters are hard to design due to significant variations in the switching frequency.

Several methods have been investigated to reduce torque ripple and flux ripple. Casadi et al. performed research and experimental tests on torque ripple analysis, including space vector modulation techniques and its discrete methods [67]. Additionally, Martins discussed a DTC switching table for multi-level inverters in [68], [69]. In [70], a dithering signal injection scheme was proposed to reduce high ripples in torque and flux. In [39], a hybrid approach to reducing torque and flux ripples while retaining switching frequency as a rough constant was discussed and tested.

5.3 Simulation Studies of Indirect Torque Controlled Interior Permanent-Magnet Drives

The controlled IPMSM proposed in this study was designed according to a PWM current-control technique. This section discusses the current-regulation and FW operations. Simulations were carried out to test the performance of this scheme. The MATLAB/SIMULINK modelling environment was used for this modelling.

A modified vector-controlled IPMSM with torque regulation was chosen from the MATLAB/SIMULINK library to investigate the performance of the flux-weakening VC scheme.

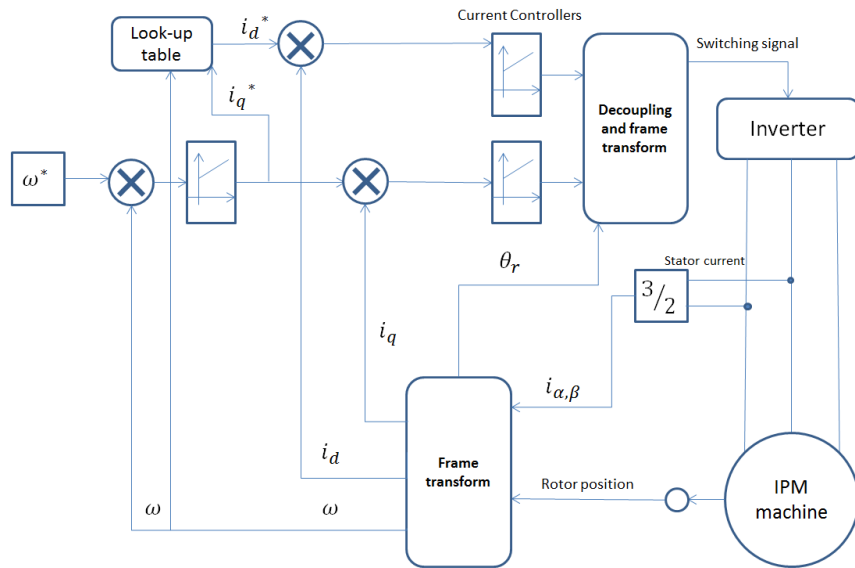


Figure 5.6. Block diagram of the interior permanent-magnet synchronous motor drive.

A modified version of the AC6 block from the SimPowerSystems electric drives library was selected for simulation purposes. It modelled a flux-weakening VC for a 100 kW, 12500 rpm, salient pole PMSM powered by a 288 VDC source. It was possible to use both speed and torque as inputs; therefore, two sets of input variables were generated for performance evaluation. Further, unit step functions were selected to simulate sudden input changes.

Table 5.4

Input speed reference

Time	Speed reference
0	300
2	-300
5	250
7	800
9	1000

Table 5.5

Input torque reference

Time	Torque reference
0	80
2	100
5	200
6.5	256
8	300

There was an assumption that permanent magnets will be mounted on the rotor surface. As a result, all PMSMs are understood to have a uniform air gap and no saliency; therefore, $L_d = L_q$. However, the PMSM in question had an interior permanent-magnet rotor; this buried-magnet configuration caused rotor saliency, with the result that $L_d > L_q$. This introduced a reluctance torque term into the PMSM torque equation. As a result, i_d was no longer set to zero because it was possible to take advantage of the reluctance torque.

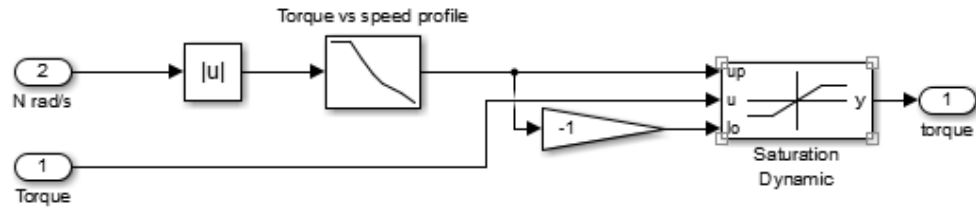


Figure 5.7. Torque limitation block.

There is an existing practical operation for regulating input torque: torque limitation block. The purpose of the block is to prevent the limitation caused by the torque speed characteristic of the motor using a 288 VDC power source. The inverter saturation mode is harnessed for this effect. If the saturation mode is activated, the desired current can no longer flow into the drive—this is because the internal machine’s voltage reaches the inverter voltage due to high desired torque for motor’s speed. This causes current tracking to be lost and a decrease in motor current . First and foremost, this block was designed to reduce reference torque as a function of the motor’s speed and the torque speed characteristic. Because of this, the inverter will not operate in saturation mode.

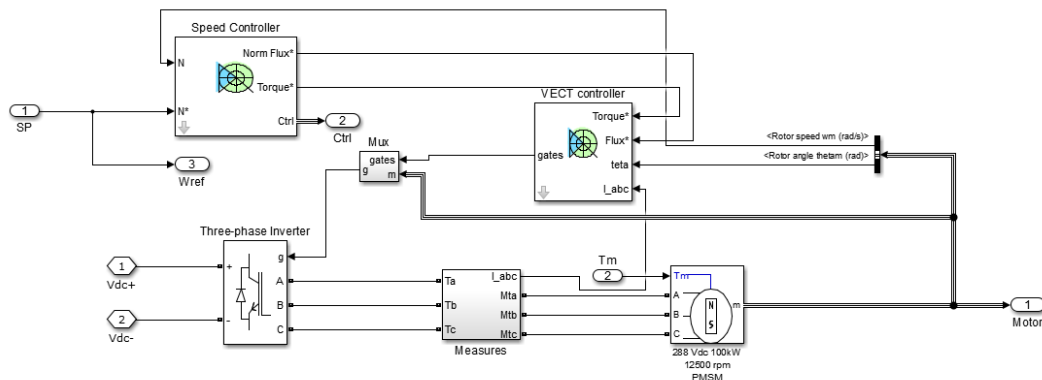


Figure 5.8. Detailed model of the interior permanent-magnet synchronous motor drive.

The PMSM drive consists of four main components: an electrical motor, a three-phase inverter, a vector controller with flux FW operations and a speed controller.

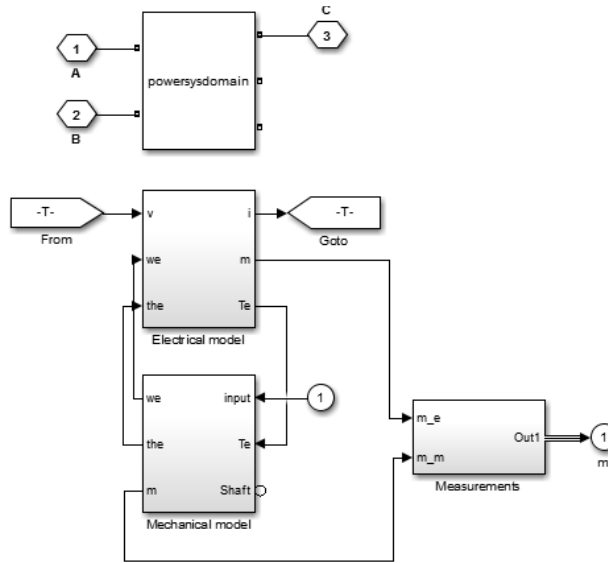


Figure 5.9. Mathematical model for the electric motor.

The electric motor used in the modelling was a 288 VDC, 100 kW PMSM. The motor had eight poles and the magnets were buried. The mathematical model was a combination of an electrical model and a mechanical model.

The three-phase inverter was a PWM-controlled VSI and the block was built by Universal Bridge Block.

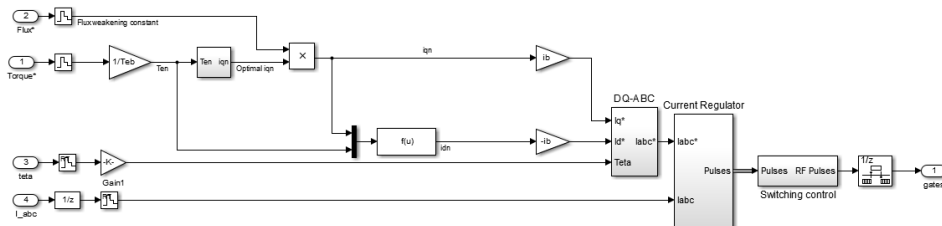


Figure 5.10. Detailed model of the vector controller.

The role of the VECT controller was to calculate the three reference motor line currents corresponding to the flux and torque references. It then generated a corresponding PWM signal through a three-phase current regulator. It was then possible to implement an optimal control scheme to minimise the line current amplitude for required torque when the nominal flux was required. Both amplitude and phase were

changed to extend the operating range of torque and speed when a flux weakening takes place.

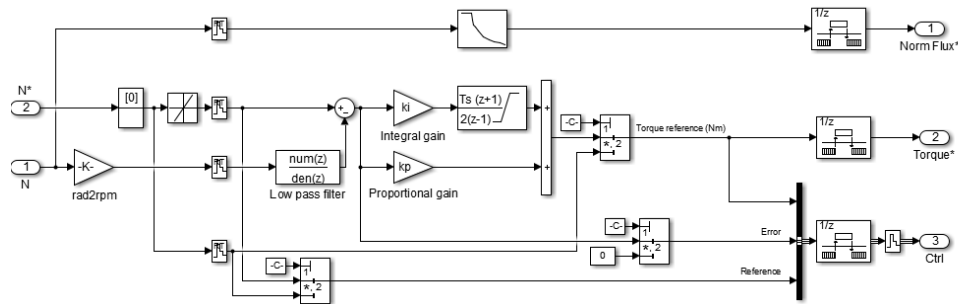


Figure 5.11. Detailed model of the speed controller.

A universal bridge block was used to simulate PWM VSI and a PI controller was used to generate reference signals for flux and torque as part of the VC block in the speed control loop. Inside the speed controller, the set point values of the rotor speed and the measured rotor speed were processed as inputs and subtracted to obtain an error signal; then, an appropriate gain was selected for the integral and proportional terms to reach steady-state outputs. As such, the output was set as the torque reference for VC. The controller implemented torque regulation and the normalised flux was computed based on the speed of the motor; this is why it was valuable to use a VECT controller for flux-weakening control.

The simulation was carried out and its parameters are outlined in Table 5.6.

Table 5.6

Parameters of the interior permanent-magnet drive and controllers

Parameter	Value
Simulation sample time	$2 \mu\text{s}$
Direct current bus voltage	288 V
Maximum switching frequency of vector controller	20 MHz
Sample time of vector controller	$2 \mu\text{s}$
Current hysteresis bandwidth	0.1 A
Sample time of speed controller	$140 \mu\text{s}$
K_P for speed controller	11 (A*sec./rad)
K_I for speed controller	16 (A*sec./rad)

For the purpose of obtaining fast responses and limited overshoot, a relatively small integral gain was selected for the speed control loop.

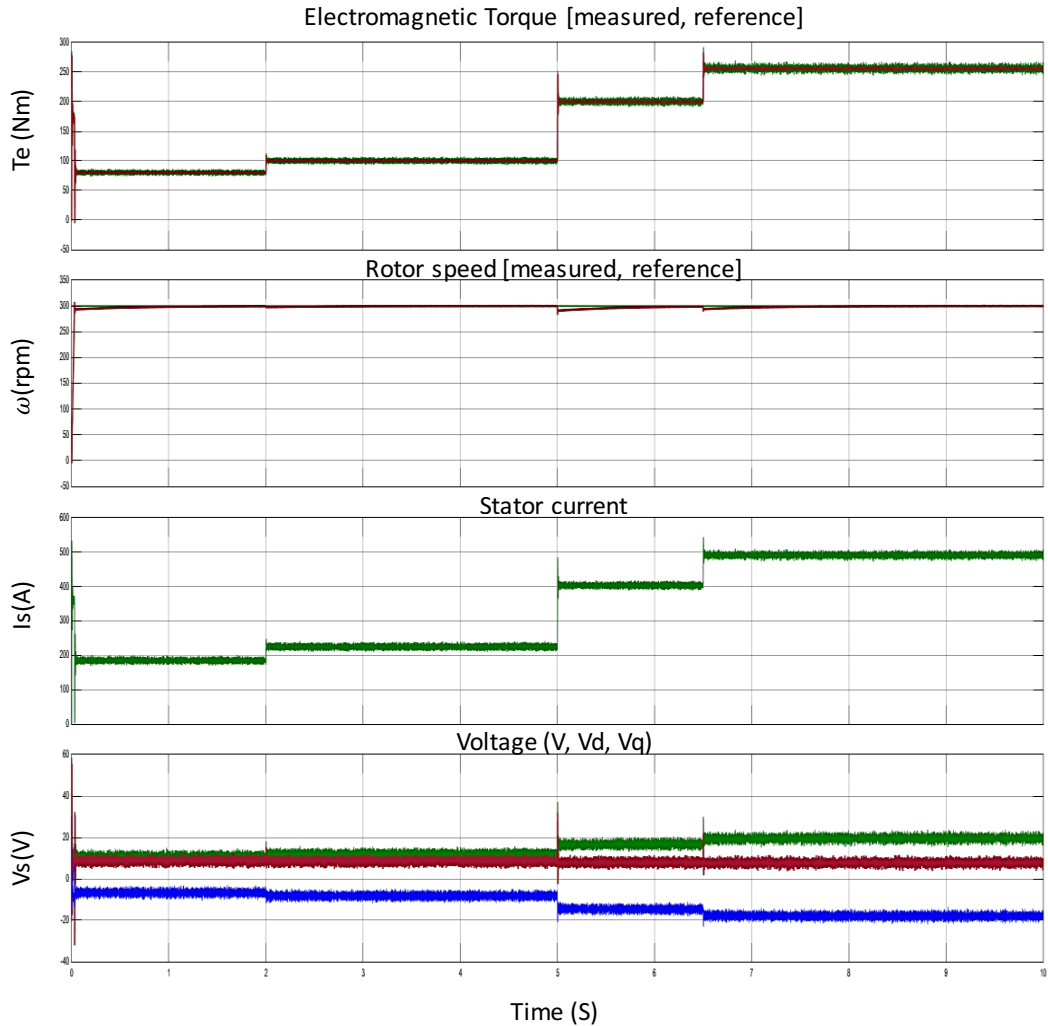


Figure 5.12. Simulation results at constant speed.

At the beginning of the simulation, the motor torque (electromagnetic and reference), rotor speed (measured value and reference), stator current magnitude and stator voltage (magnitude, V_d and V_q) were monitored and displayed in the external scope.

Because of the variable torque demand, the electromagnetic torque changed with the torque reference. A flux weakening was activated to limit the motor's back-EMF and maintain constant speed; thus, I_d increased with the negative phase. Conversely, the reference torque was limited as a product of the motor's torque speed characteristic to

prevent inverter saturation, which caused I_q to decrease. The magnitude of the current was constant and only the angle changed.

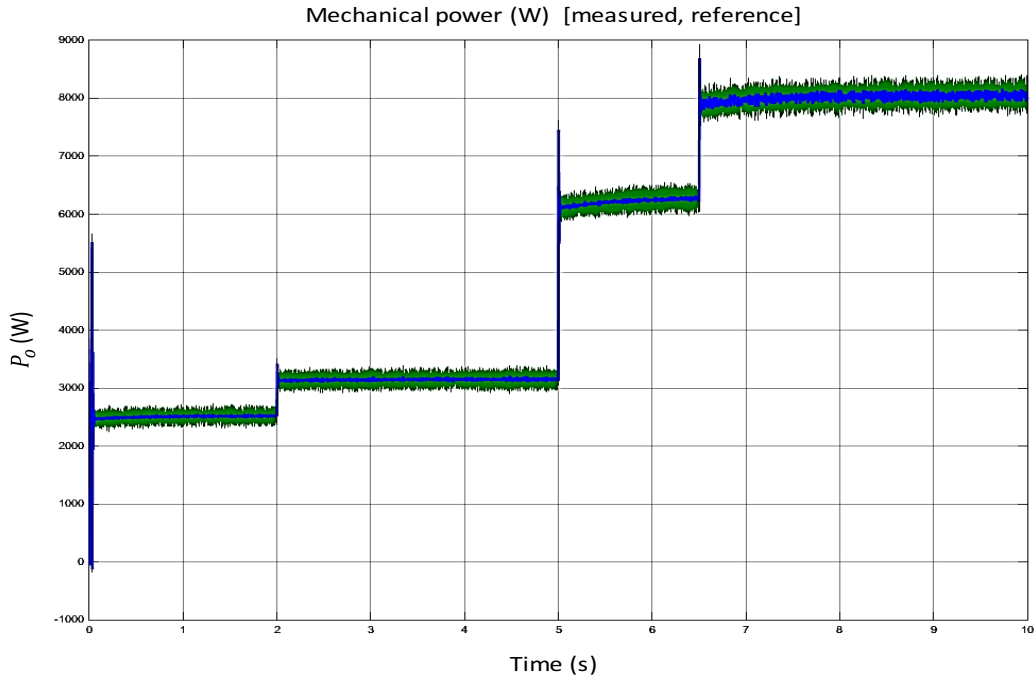


Figure 5.13. Power output at constant speed.

The higher torque demand led to higher mechanical power output. Figure 5.14 shows that the measured power consistently and precisely followed the reference signal, except when an overshoot was caused by load disturbance. However, the time of the response was less than 0.06 s.

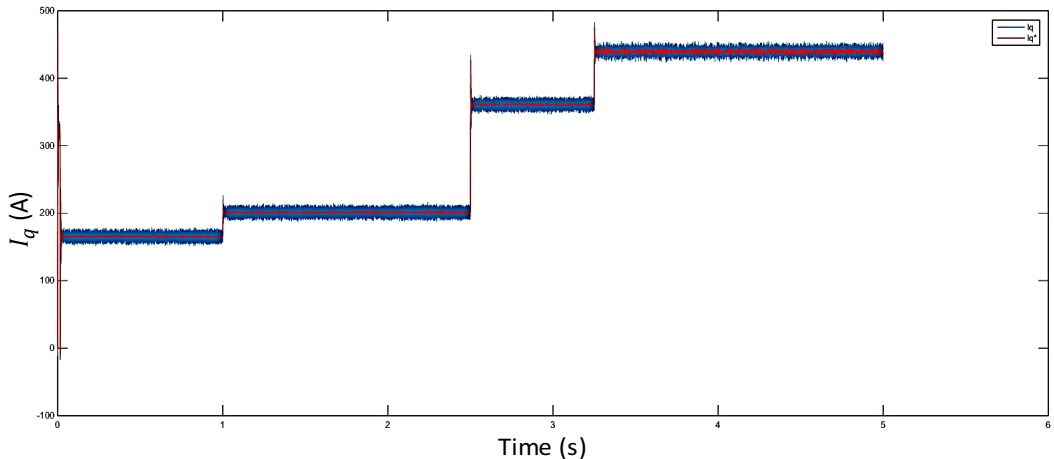


Figure 5.14. i_q current vector response.

Figures 5.14–5.16 show the controlled current vector response to the input signal.

The reference d -axis current changed according to varying torque demands; hence, a flux weakening was performed to limit the motor's back-EMF. This increased the negative i_d current component. The reference torque was limited by the motor's torque speed characteristic to prevent inverter saturation, which caused the q current component to decrease. The magnitude of the current was constant—only the angle changed.

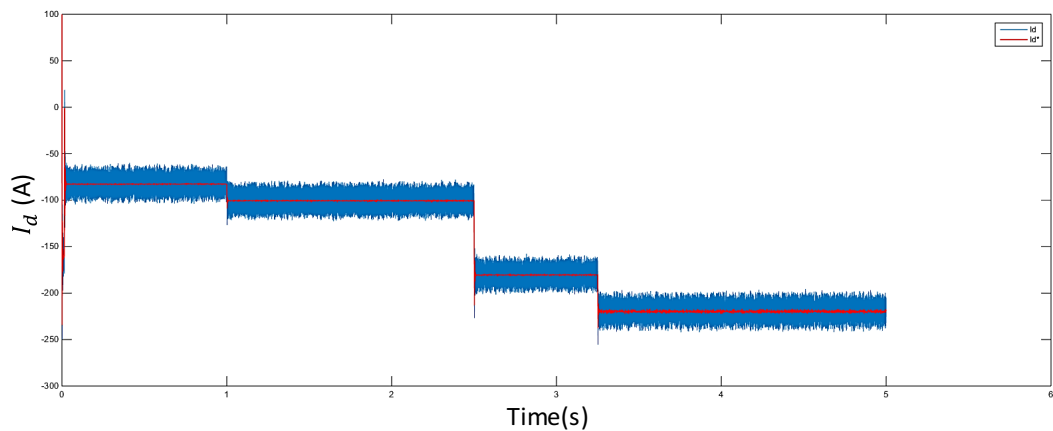


Figure 5.15. i_d current vector response.

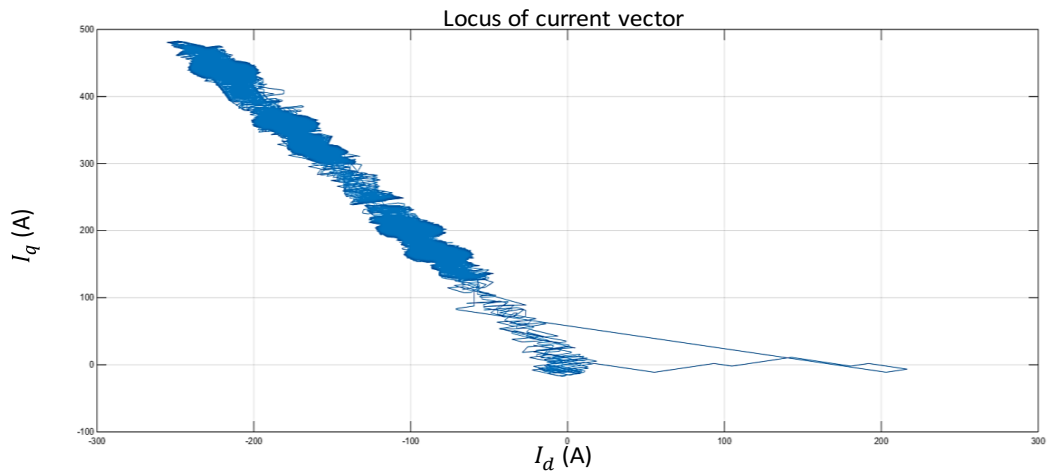


Figure 5.16. Locus of both current vectors.

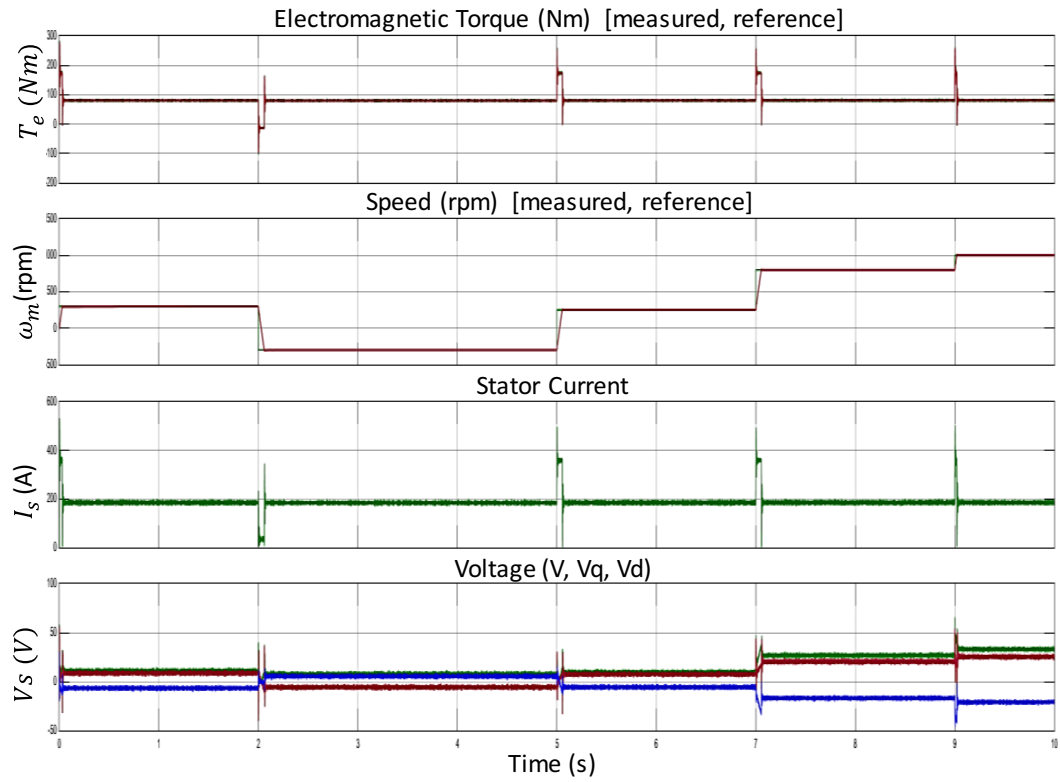


Figure 5.17. *Simulation results at constant torque reference.*

As outlined in Table 5.4, the speed reference was simulated as a step signal with different amplitudes. The control loop was able to track the reference value consistently. Although the speed reference changed sharply—for example, at 2 s and 7 s—the output torque was still able to track the constant torque reference. The transient time was less than 0.06 s and the overshoot was relatively limited. At 7 s, the rotor speed exceeded the nominal speed of 3000 rpm; hence, a flux weakening was performed to limit the motor's back-EMF. As a result, the i_d current component increased negatively.

Figure 5.18 shows that changes in the reference speed caused the output power to decrease at 2 s and then increase to meet the load demand.

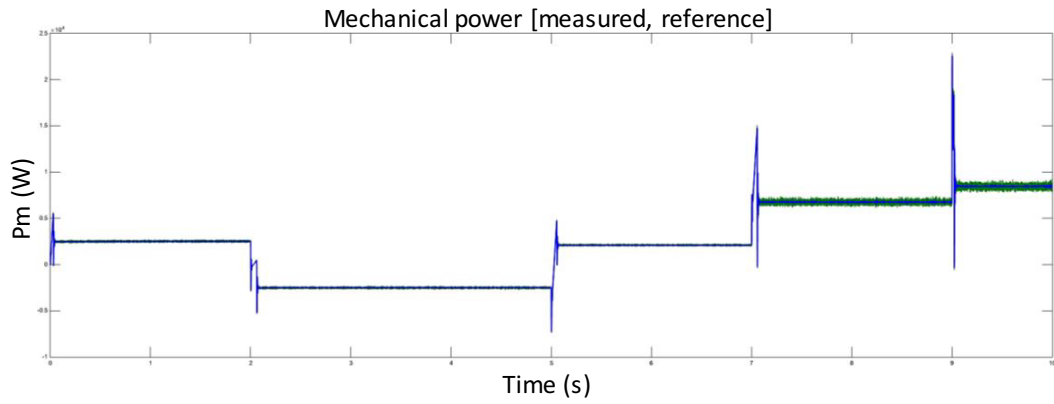


Figure 5.18. Mechanical power at constant load torque.

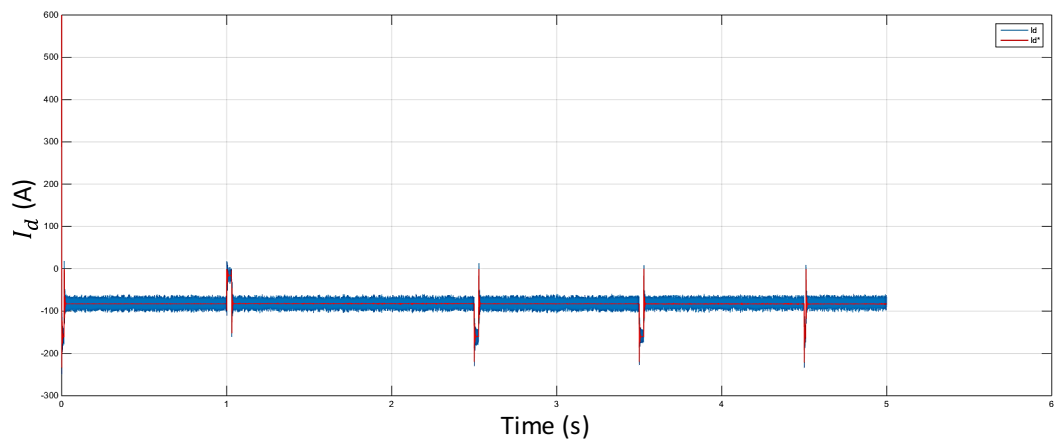


Figure 5.19. i_d current response.

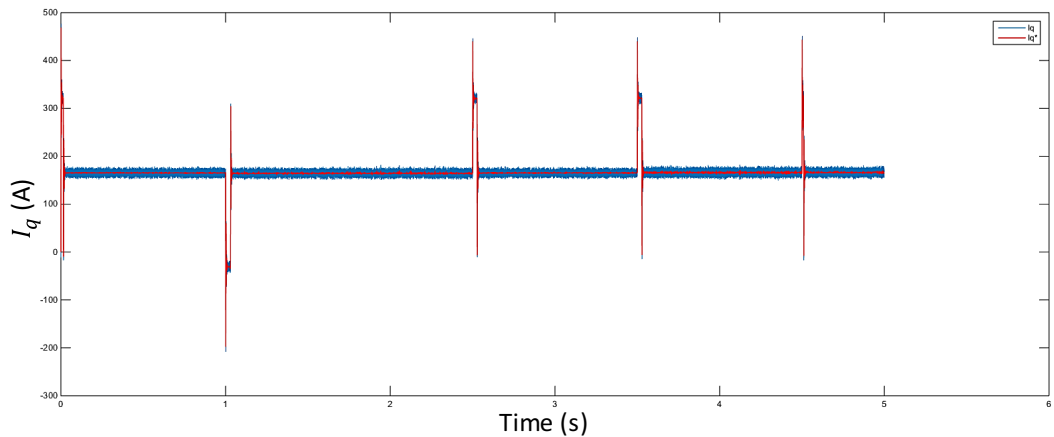


Figure 5.20. i_q current response.

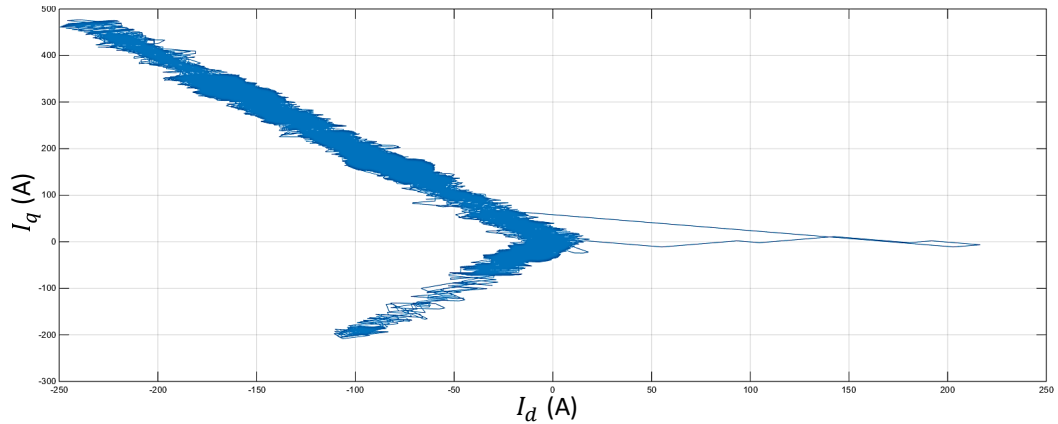


Figure 5.21. Locus of i_d and i_q vectors.

The reference speed changed with time (see Table 5.5). The reference torque was restricted due to the motor's torque speed characteristic. The I_q current component decreased at 1 s to prevent inverter saturation. The magnitude of the current was maintained at a constant value, but the phase of the current changed.

5.4 Development of the Motor Control Test Bench

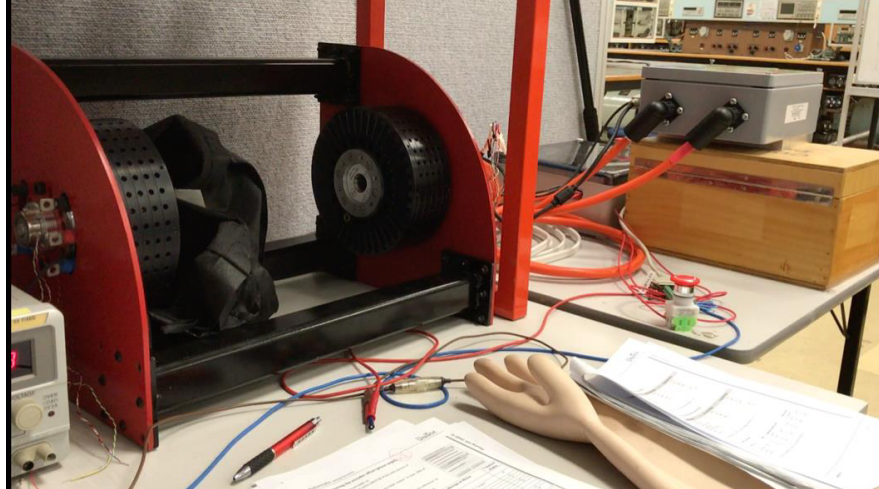


Figure 5.22. University of Tasmania Formula SAE motor bench test platform.

A test bench was developed in-house to assist with validating the simulation data. Figure 5. shows the test bench setup, which consisted of a motor mounting frame, two 80 kW electric motors, inverters, a safety protection circuit, and a data logger. The torque transducer and the mechanical coupling of the twin motor configuration was not complete at the time of the picture due to time constraints. The data collection, fine-tuning of the

inverter and the comparison of the simulation and physical data will be essential parts of future investigations, which is discussed in Chapter 6.

Chapter 6: Conclusion and Future Research

6.1 Conclusions

This thesis presented a comprehensive review of EV traction systems and various motor control strategies. It also discussed the results of simulations carried out to compare the performance of different control methods. This research provides a foundation to further develop the proposed longitudinal torque control system and its integrated motor control system.

This thesis also examined the several control techniques that have recently been proposed for PMSMs. It discussed cover control theory, control algorithms, the advantages and disadvantages of each technique and whether they had been investigated analytically and mathematically.

To fully evaluate the PMSM control strategies, two different rotor structures were introduced. As a part of this, VC and the basic DTC for PMSM drives were described, and a review of the literature was presented.

This thesis also evaluated various PMSM models. Vector space theory was used to model the DTC control scheme to ensure high performance of the proposed DTC PMSM drive. Further, the motor model was described in terms of a three-phase stationary frame and a two-phase reference frame. The equations were derivated based on per-unit values when analysing the different control strategies. This simplified the process of generalisation and comparison for both control techniques.

This thesis also reported on simulations carried out regarding various control strategies. A comparison of the torque response under the DTC and VC was employed as part of this process. The DTC method was shown to have several benefits, including fast torque control, simple implementation and less transformation of reference frames and current-control loops.

A methodology for designing EVs was introduced in Chapter 4 and subsequently validated in simulation.

6.2 Future Research

This thesis provides a foundation for understanding and developing a traction controller with an integrated motor control system. There is significant scope for additional research to further investigate the proposed traction controller and undertake additional testing to validate the various control methods discussed.

6.2.1 Simulation works

Further simulation works might involve:

- developing the MF tyre model and the QV model to create vehicle models as part of the working plant
- integrating the vehicle model with the established PMSM model to create the final working plant
- using the developed DTC motor controller to conduct open-loop simulation for the entire working plant and validating results with comparison to existing literatures
- implement PID controller for the close loop velocity control of by setting reference motor torque
- reviewing and simulating other control methods (e.g., the sliding model, fuzzy logic and maximum transmissible torque estimation control methods), then comparing their performance
- selecting a control method based on the results obtained and integrating a DTC controller as a subsystem in the SIMULINK environment to create a master controller.

6.2.2 Physical data collection and comparison study

Further data collection and comparison might involve:

- completing the test bench by installing a torque transducer and data logger
- using SIMULINK to convert the master controller to hardware for hardware-in-loop simulation and data collection
- collaborating with the UTAS FSAE team to modify an existing vehicle to a physical test platform to validate the data against track data.

References

- [1] Y. Zhuoping, F. Yuan, and X. Lu, “Review on Vehicle Dynamics Control of Distributed Drive Electric Vehicle,” *J. Mech. Eng.*, vol. 49, no. 8, p. 49, 2013.
- [2] V. Ivanov, D. Savitski, and B. Shyrokau, “A Survey of Traction Control and Anti-lock Braking Systems of Full Electric Vehicles with Individually-Controlled Electric Motors,” *IEEE Trans. Veh. Technol.*, vol. 9545, no. c, pp. 1–1, 2014.
- [3] P. N. Huu, “Design of an electronic differential for a formula electric racecar,” *Proc. 2013 IEEE Int. Electr. Mach. Drives Conf. IEMDC 2013*, pp. 62–66, 2013.
- [4] S. Murata, “Innovation by in-wheel-motor drive unit,” *Veh. Syst. Dyn.*, vol. 50, no. 6, pp. 807–830, 2012.
- [5] Y. Hori, Y. Toyoda, and Y. Tsuruoka, “Traction Control of Electric Vehicle: Basic Experimental Results Using the Test EV UOT Electric March,” *IEEE Trans. Ind. Appl.*, vol. 34, no. 5, pp. 1131–1138, 1998.
- [6] T. Jeong *et al.*, “Current Harmonics Loss Analysis of 150-kW Traction Interior Permanent Magnet Synchronous Motor Through Co-Analysis of - Axis Current Control and Finite Element Method,” vol. 49, no. 5, pp. 2343–2346, 2013.
- [7] Woosuk Sung, Jincheol Shin, and Yu-seok Jeong, “Energy-Efficient and Robust Control for High-Performance Induction Motor Drive With an Application in Electric Vehicles,” *IEEE Trans. Veh. Technol.*, vol. 61, no. 8, pp. 3394–3405, 2012.
- [8] Y. P. Yang and C. P. Lo, “Current distribution control of dual directly driven wheel motors for electric vehicles,” *Control Eng. Pract.*, vol. 16, no. 11, pp. 1285–1292, 2008.
- [9] F. D. R. Car, D. Bohl, N. Kariotoglou, A. B. Hempel, P. J. Goulart, and J. Lygeros, “Model-Based Current Limiting for Traction Control of an Electric,” *2014 Eur. Control Conf.*, pp. 1981–1986, 2014.

- [10] D. Yin, S. Oh, and Y. Hori, “A novel traction control for EV based on maximum transmissible torque estimation,” *IEEE Trans. Ind. Electron.*, vol. 56, no. 6, pp. 2086–2094, 2009.
- [11] H. B. Pacejka and E. Bakker, “The magic formula tyre model,” *Veh. Syst. Dyn.*, 1992.
- [12] J. Gerdes, C. Wilson, and D. Bevly, “The Use of GPS Based Velocity Measurements for Measurement of Sideslip and Wheel Slip,” *Veh. Syst. Dyn. - VEH SYST DYN*, vol. 38, pp. 127–147, 2003.
- [13] Fredrik Gustafsson, “Adaptive Filtering,” in *Adaptive Filtering and Change Detection*, John Wiley & Sons, Ltd, 2001, pp. 111–204.
- [14] K. Fujii and H. Fujimoto, “Traction control based on slip ratio estimation without detecting vehicle speed for electric vehicle,” in *Fourth Power Conversion Conference-NAGOYA, PCC-NAGOYA 2007 - Conference Proceedings*, 2007.
- [15] M. Amodeo, A. Ferrara, R. Terzaghi, and C. Vecchio, “Wheel Slip Control via Second-Order Sliding-Mode Generation,” *Trans. Intell. Transp. Sys.*, vol. 11, no. 1, pp. 122–131, Mar. 2010.
- [16] Y. Hori, “Future vehicle driven by electricity and control - Research on four-wheel-motored ‘UOT Electric March II,’” *IEEE Trans. Ind. Electron.*, vol. 51, no. 5, pp. 954–962, 2004.
- [17] F. R. Committee, “2017-18 Formula SAE ® Rules,” 2017.
- [18] C. Iurian, F. Ikhouane, J. J. Rodellar Benedé, and R. Griñó, “Identification of a system with dry friction,” *Reports Recer. l’Institut d’Organització i Control Sist. Ind.*, 2005.
- [19] B. Armstrong-Hélouvry, P. Dupont, and C. C. De Wit, “A survey of models, analysis tools and compensation methods for the control of machines with friction,” *Automatica*, vol. 30, no. 7, pp. 1083–1138, 1994.

- [20] C. C. de Wit, P. Lischinsky, K. J. Åström, and H. Olsson, “A New Model for Control of Systems with Friction,” *IEEE Trans. Automat. Contr.*, 1995.
- [21] C. Canudas De Wit and P. Tsotras, “Dynamic tire friction models for vehicle traction control,” *Proc. 38th IEEE Conf. Decis. Control (Cat. No.99CH36304)*, vol. 4, no. December, pp. 3746–3751, 1999.
- [22] D. Haessig and B. Friedland, “On the Modeling and Simulation of Friction,” in *Journal of Dynamic Systems Measurement and Control-transactions of The Asme - J DYN SYST MEAS CONTR*, 1990, vol. 1482, pp. 1256–1261.
- [23] Y. F. Liu, J. Li, Z. M. Zhang, X. H. Hu, and W. J. Zhang, “Experimental comparison of five friction models on the same test-bed of the micro stick-slip motion system,” *Mech. Sci.*, vol. 6, no. 1, pp. 15–28, 2015.
- [24] J. L. Harned, L. E. Johnston, and G. Scharpf, “Measurement of Tire Brake Force Characteristics as Related to Wheel Slip (Antilock) Control System Design,” *SAE Trans.*, vol. 78, pp. 909–925, 1969.
- [25] C. Canudas-de-Wit, P. Tsotras, E. Velenis, M. Basset, and G. Gissinger, “Dynamic friction models for road/tire longitudinal interaction,” *Vehicle System Dynamics*. 2003.
- [26] H. E. Tseng and D. Hrovat, “State of the art survey: Active and semi-active suspension control,” *Veh. Syst. Dyn.*, 2015.
- [27] Z. Cai, C. Ma, and Q. Zhao, “Acceleration-to-torque ratio based anti-skid control for electric vehicles,” in *Proceedings of 2010 IEEE/ASME International Conference on Mechatronic and Embedded Systems and Applications, MESA 2010*, 2010.
- [28] K. Fujii and H. Fujimoto, “Traction control based on slip ratio estimation without detecting vehicle speed for electric vehicle,” *Fourth Power Convers. Conf. PCC-NAGOYA 2007 - Conf. Proc.*, pp. 688–693, 2007.

- [29] E. Haque, "Improvements of A Direct Torque Controller of an Interior Permanent Magnet Synchronous Motor Drive," The University of New South Wales, 2002.
- [30] F. Blaschke, "Principle of field orientation as used in the new Transvektor control system for induction machines," *Siemens-Z*, vol. 45, no. 10, pp. 757–760, 1971.
- [31] M. F. Rahman, L. Zhong, and K. W. Lim, "A direct torque-controlled interior permanent magnet synchronous motor drive incorporating field weakening," *IEEE Trans. Ind. Appl.*, 1998.
- [32] I. Takahashi and T. Noguchi, "A New Quick-Response and High-Efficiency Control Strategy of an Induction Motor," *IEEE Trans. Ind. Appl.*, 1986.
- [33] I. Takahashi and Y. Ohmori, "High-Performance Direct Torque Control of an Induction Motor," *IEEE Trans. Ind. Appl.*, 1989.
- [34] Y.-C. Chang, J.-T. Chan, J.-C. Chen, and J.-G. Yang, "Development of permanent magnet synchronous generator drive in electrical vehicle power system," in *2012 IEEE Vehicle Power and Propulsion Conference, VPPC 2012*, 2012, pp. 115–118.
- [35] S. Dwivedi and B. Singh, "Vector control vs Direct Torque Control comparative evaluation for PMSM drive," in *2010 Joint International Conference on Power Electronics, Drives and Energy Systems, PEDES 2010 and 2010 Power India*, 2010.
- [36] V. Vector, S. Strategy, I. P. Dtc, and G. Dieter, "Voltage Vector Selection Strategy for the Interior PMSM DTC System II Control of stator flux , torque angle and torque," *Control*, 2011.
- [37] A. Panday and H. O. Bansal, "A Review of Optimal Energy Management Strategies for Hybrid Electric Vehicle," *Int. J. Veh. Technol.*, vol. 2014, p. 160510, 2014.
- [38] T. Finken, M. Hombitzer, and K. Hameyer, "Study and comparison of several permanent-magnet excited rotor types regarding their applicability in electric

- vehicles,” in *2010 Emobility - Electrical Power Train, EEPT 2010*, 2010.
- [39] L. Tang Electrical Engineering & Telecommunications, Faculty of Engineering, UNSW, “An improved direct torque controlled interior permanent magnet synchronous machine drive without a speed sensor.” 2004.
 - [40] S. Ozcira, N. Bekiroglu, and E. Aycicek, “Speed control of permanent magnet synchronous motor based on direct torque control method,” in *2008 International Symposium on Power Electronics, Electrical Drives, Automation and Motion*, 2008, pp. 268–272.
 - [41] P. Pillay, “Vector control of AC permanent magnet machines,” in *1989 Fourth International Conference on Electrical Machines and Drives Conf. Publ. No. ??*), 1989, pp. 293–297.
 - [42] G. Champenois, P. Mollard, and J. P. Rognon, “Effective digital torque control systems for permanent magnets converter fed sinusoidal synchronous machines,” in *Conference Record of the 1988 IEEE Industry Applications Society Annual Meeting*, 1988, pp. 259–265 vol.1.
 - [43] Y. Takeda and T. Hirasa, “Current phase control methods for permanent magnet synchronous motors considering saliency,” in *PESC '88 Record., 19th Annual IEEE Power Electronics Specialists Conference*, 1988, pp. 409–414 vol.1.
 - [44] S. Morimoto, K. Hatanaka, Y. Tong, Y. Takeda, and T. Hirasa, “Servo drive system and control characteristics of salient pole permanent magnet synchronous motor,” *IEEE Trans. Ind. Appl.*, vol. 29, no. 2, pp. 338–343, 1993.
 - [45] S. Morimoto, Y. Takeda, K. Hatanaka, Y. Tong, and T. Hirasa, “Design and control system of inverter-driven permanent magnet synchronous motors for high torque operation,” *IEEE Trans. Ind. Appl.*, vol. 29, no. 6, pp. 1150–1155, 1993.
 - [46] D. Finney, “Vector Control of AC Machines,” *Power Eng. J.*, 1992.
 - [47] T. M. Jahns, G. B. Kliman, and T. W. Neumann, “Interior Permanent-Magnet

- Synchronous Motors for Adjustable-Speed Drives," *IEEE Trans. Ind. Appl.*, 1986.
- [48] B. K. Bose, "A high-performance inverter-fed drive system of an interior permanent magnet synchronous machine," *IEEE Trans. Ind. Appl.*, vol. 24, no. 6, pp. 987–997, 1988.
- [49] L. Zhong, M. F. Rahman, W. Y. Hu, and K. W. Lim, "Analysis of direct torque control in permanent magnet synchronous motor drives," *IEEE Trans. Power Electron.*, 1997.
- [50] M. R. Zolghadri, G. Pelissou, and D. Roye, *Start up of a global direct torque control system*. 1996.
- [51] M. R. Zolghadri, J. Guiraud, J. Davoine, and D. Roye, "A DSP based direct torque controller for permanent magnet synchronous motor drives," in *PESC 98 Record. 29th Annual IEEE Power Electronics Specialists Conference (Cat. No.98CH36196)*, 1998, vol. 2, pp. 2055–2061 vol.2.
- [52] S. Dan, W. Fang, and H. Yikang, *Study on the direct torque control of permanent magnet synchronous motor drives*. 2001.
- [53] R. Zaimeddine and E. M. Berkouk, "Switching strategies in direct torque control using a three-level voltage source inverter," vol. 4, pp. 736–744, Jun. 2005.
- [54] M. Fu and L. Xu, "A sensorless direct torque control technique for permanent magnet synchronous motors," in *Conference Record of the 1999 IEEE Industry Applications Conference. Thirty-Forth IAS Annual Meeting (Cat. No.99CH36370)*, 1999, vol. 1, pp. 159–164 vol.1.
- [55] H. Yuwen, T. Cun, G. Yikang, Y. Zhiqing, L. X. Tang, and M. F. Rahman, *In-depth research on direct torque control of permanent magnet synchronous motor*. 2002.
- [56] A. S. Al-Adsani and N. Schofield, "Hybrid permanent magnet generators for electric vehicle applications," *2009 IEEE Int. Electr. Mach. Drives Conf.*, pp.

- 1754–1761, May 2009.
- [57] A. Ahmed and D. D. Bhutia, “Propulsion System Design and Sizing of an Electric Vehicle,” *Int. J. Electron. Electr. Eng.*, vol. 3, no. 1, pp. 14–18, 2014.
- [58] I. Alcala, A. Claudio, and G. Guerrero, “Analysis of propulsion systems in electric vehicles,” in *2005 2nd International Conference on Electrical and Electronics Engineering*, 2005, no. Cie, pp. 309–313.
- [59] A. Emadi, *Advanced Electric Drive Vehicles*. 2015.
- [60] X. W. Gong, D. J. Wu, and J. Ma, “Matching Design and Simulation of Powertrain Parameters for Electric Vehicles,” *Adv. Mater. Res.*, vol. 655–657, no. 1, pp. 596–602, 2013.
- [61] N. Hashernnia and B. Asaei, “Comparative Study of Using Different Electric Motors in the Electric Vehicles,” in *International Conference on Electrical Machines*, 2008, no. c, pp. 1–5.
- [62] R. Yang, N. Schofield, and A. Emadi, “Comparative study between interior and surface permanent magnet traction machine designs,” *2016 IEEE Transp. Electrif. Conf. Expo, ITEC 2016*, pp. 1–6, 2016.
- [63] L. Kumar and S. Jain, “Electric propulsion system for electric vehicular technology: A review,” *Renew. Sustain. Energy Rev.*, vol. 29, pp. 924–940, 2014.
- [64] “OptimumDynamics | OptimumG.” [Online]. Available: <https://optimumg.com/product/optimumdynamics/>. [Accessed: 03-Feb-2020].
- [65] M. E. Haque, L. Chong, and M. F. Rahman, *The effect of offset error and its compensation for a direct torque controlled interior permanent magnet synchronous motor drive*. 2001.
- [66] M. E. Haque, L. Zhong, and M. F. Rahman, “A Sensorless Initial Rotor Position Estimation Scheme for a Direct Torque Controlled Interior Permanent Magnet Synchronous Motor Drive,” *IEEE Trans. Power Electron.*, 2003.

- [67] D. Casadei, G. Serra, and A. Tani, “Analytical investigation of torque and flux ripple in DTC schemes for induction motors,” *IECON Proc. (Industrial Electron. Conf.)*, 1997.
- [68] C. A. Martins, X. Roboam, T. A. Meynard, and A. S. Carvalho, “Switching frequency imposition and ripple reduction in DTC drives by using a multilevel converter,” *IEEE Trans. Power Electron.*, 2002.
- [69] A. BenAbdelghani, C. A. Martins, X. Roboam, and T. A. Meynard, “Use of extra degrees of freedom in multilevel drives,” *IEEE Trans. Ind. Electron.*, 2002.
- [70] T. Noguchi, M. Yamamoto, S. Kondo, and I. Takahashi, “Enlarging switching frequency in direct torque-controlled inverter by means of dithering,” *IEEE Trans. Ind. Appl.*, 1999.